Control-Oriented Modeling of Wireless Power Transfer Systems With Phase-Shift Control

Fengwei Chen, Hugues Garnier, Qijun Deng, Marian K. Kazimierczuk, *Fellow, IEEE*, and Xiangtao Zhuan

***Abstract*—This paper is concerned with control-oriented modeling of a class of wireless power transfer systems with a phase-shift-controlled inverter. Two methods are investigated: the analytical modeling method, which is based on physical laws, and the refined instrumental variable method, which is based on sampled data. It shows that the former provides physical insights into the system, and that the resulting models will be accurate if the true circuit component parameters are *a priori* known. Otherwise, the model accuracy may decline. By contrast, the latter provides a cheap solution for accurate modeling, based only on a set of sampled input–output data, and the resulting model can capture very well the dynamic behavior of the system within a defined operating range. In real applications, it is always hard to know the actual circuit component parameters, since they may drift from the nominal values, due to some reasons such as the aging of circuit components and the variation of coil placement, making the analytical modeling method not very accurate. Therefore, to preserve the virtues of both methods, it is suggested to use them as a combination, that is, using the analytical modeling method to determine the model structure while using the data-driven modeling method to estimate the model parameters. All results derived in this paper are verified by means of both numerical simulation and experimental validation.**

***Index Terms*—Data-driven modeling, instrumental variable (IV), system identification, time delay, wireless power transfer (WPT).**

I. Introduction

WIRELESS power transfer (WPT) based on magnetic resonant coupling is a promising technology for delivering electric energy and has gained an increasing attention in the fields of both scientific research and industrial practice in the last decade. Among the merits of WPT, the most fascinating one is that it has no physical contacts, which enables us to obtain improved robustness, reliability, and mobility in a wide spectrum of applications such as electric vehicles [10], [26], portable devices, and household appliances, to name a few. Several techniques have been used to implement WPT, as surveyed in [20] and [22]. Among these, radiative transfer and resonant coupling have been well known. The former has long been used to transfer signals, but has very low efficiency for transferring power due to its omnidirectional radiation nature. By contrast, resonant coupling is more suited to high-power applications and, therefore, will be adopted in this paper.

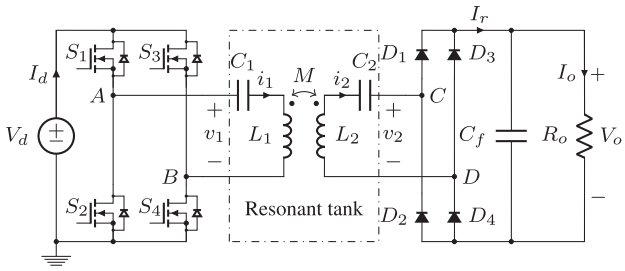

Fig. 1. Circuit topology for WPT under consideration.

A series–series compensated WPT system consisting of three stages is considered; see Fig. 1 for the circuit topology. The input stage is a phase-shift-controlled full-bridge inverter that converts the dc voltage to a high-frequency square wave. Then, in the second stage, energy is transferred from one side to another through a resonant tank composed of two coupled inductors L_1 and L_2. As the two coils are loosely coupled, i.e., the magnetizing inductance is small, while the leakage inductance is large, a capacitor C_1 is connected in series with L_1 to compensate for the inductive behavior of the sending resonator, and the same is done to the receiving resonator. This series–series compensation strategy has the merit that the choice of the compensating capacitor is independent of the load [39]. Moreover, both sides of the resonant tank need to oscillate around the switching frequency in order to maximize the rate of energy transfer [2], [28]. The last stage is a low-pass filter, where, in order to attenuate ripples of the output voltage V_o, as well as to remain compact in the filter size, only a single capacitor C_f is used.

The typical waveforms of the signals in the resonant tank are shown Fig. 2, where v_{s_1}–v_{s_4} designate the control signals for switches S_1–S_4, respectively, v_1 and i_1 are the input voltage and current of the resonant tank, respectively, and v_2 and i_2 are the

Manuscript received December 20, 2018; revised April 5, 2019; accepted May 30, 2019. Date of publication June 4, 2019; date of current version November 12, 2019. This work was supported in part by the National Natural Science Foundation of China under Grants 61703311 and 51677139, in part by the China Postdoctoral Science Foundation under Grant 2017M620335, and in part by the Shenzhen Science and Technology Innovation Committee under Grants JCYJ2017081811280674 and JCYJ20170818144449801. Recommended for publication by Associate Editor O. Lucia. *(Corresponding author: Qijun Deng.)*

F. Chen is with the Department of Automation, School of Electrical Engineering and Automation, Wuhan University, Wuhan 430072, China (e-mail: fengwei.chen@whu.edu.cn).

H. Garnier is with the Centre de Recherche en Automatique de Nancy, Centre National de la Recherche Scientifique, Université de Lorraine, F-54000 Nancy, France (e-mail: hugues.garnier@univ-lorraine.fr).

Q. Deng and X. Zhuan are with the Department of Automation, School of Electrical Engineering and Automation, Wuhan University, Wuhan 430072, China, and also with the Shenzhen Research Institute, Wuhan University, Shenzhen 518057, China (e-mail: dqj@whu.edu.cn; xtzhuan@whu.edu.cn).

M. K. Kazimierczuk is with the Department of Electrical Engineering, Wright State University, Dayton, OH 45435 USA (e-mail: marian.kazimierczuk@wright.edu).

Color versions of one or more of the figures in this paper are available online at http://ieeexplore.ieee.org.

Digital Object Identifier 10.1109/TPEL.2019.2920863

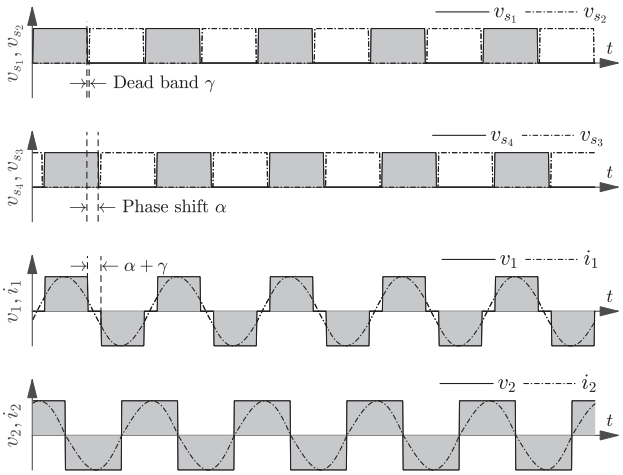

Fig. 2. Normalized waveforms of the signals in Fig. 1. v_{s_1}–v_{s_4} are control signals for switches S_1–S_4, respectively. v_1 and i_1 are the input voltage and current of the resonant tank, respectively. v_2 and i_2 are the output voltage and current of the resonant tank, respectively.

output voltage and current of the resonant tank, respectively. As the switches are not ideal components, a dead band γ is inserted before they are switched ON. The phase shift α between the leading leg (S_1 and S_2) and the lagging leg (S_3 and S_4) is considered as the control variable to regulate the output voltage V_o. As α varies from 0 to π, V_o decreases from the maximum to zero.

In practical applications, a WPT system is always operated in closed loop with a controller to prevent the output voltage from drifting too far from the set point. Generally speaking, there are two main strategies to regulate the output voltage, namely, frequency control and phase-shift control. It is known that the former often complicates the design of electromagnetic interference filters [32], while the latter does not suffer from this problem, since it works at a constant switching frequency. This explains why a phase-shift-controlled full-bridge inverter is used as the input stage in Fig. 1. See also [8], [9], and [21] for further properties of inverters of this type.

Accurate models of WPT systems are always desired in control system design to improve the achievable performance. In the field of power electronics, mathematical models are usually established by using physical laws, e.g., Kirchoff's laws. In these methods, it is often assumed that the system is at a steady state such that the signals in the resonant tank can be approximated by their first harmonic [12], [13], [39], [41]. Under this assumption, the original circuit has a first harmonic equivalent, and, based on which, the underlying nonlinear model (i.e., large-signal model) can be derived easily. On the other hand, since many mature control design methodologies are based on linear models, the resulting nonlinear large-signal model needs to be linearized at a static operating point to obtain a linear small-signal model.

In the laboratory environment, the conventional methods can be accurate, since the true circuit component parameters are *a priori* known or can be precisely measured. Unfortunately, it is not the case for real industrial applications, where the system is continuously running. Due to the aging effect of the circuit components, the variation of the coil placement, or the change of the load impedance, the actual component parameters may drift from the nominal ones. Meanwhile, measurement of these parameters may be technically hard or very expensive due to economic and safety reasons. In this case, the conventional methods may fail to yield accurate models and, thus, are not an optimal choice for dynamic model tracking [33].

To circumvent the above-mentioned problem, an alternative data-driven modeling method will be proposed to infer models for WPT systems. This method has some advantages compared to conventional methods in the following two aspects. First, it is based on sampled input–output data that are relatively easy to obtain, rather than the true circuit component parameters. Second, the model parameters are estimated by minimizing a quadratic loss function defined by the mean-squared errors between the measured and predicted outputs. Hence, within the defined operating range, the resulting model best explains the data in the mean-squared error sense. By contrast, conventional methods often rely on first harmonic approximation and linearization, which may lead to a loss in the model accuracy, particularly in the presence of large harmonic distortions [40]. From the above discussion, data-driven modeling can be a cheap and effective alternative for accurate dynamic model tracking: when a new model is wanted, the user has to collect a new set of input–output data and then repeat the estimation procedure to update the model parameters.

Data-driven modeling, known as system identification in the control literature, is the field of inferring mathematical models from experimental data [24], [31]. It is an effective solution to overcome the drawbacks of conventional methods, which result in models that are often complex and not easily estimated from the experimental data because of identifiability problems caused by overparameterization. This is also the main reason limiting their use in control system design [16]. By contrast, data-driven modeling is able to yield relatively simple models that can well describe the behavior of the system within a defined operating range. In this paper, a parameterized gray- or black-box model is used to characterize the behavior of a WPT system, and in the model estimation phase, one needs to solve the problem of how to determine the model order and how to estimate the model parameters. If no *a priori* knowledge about this is available, model order selection is usually done by trial and error in the system identification literature. Fortunately, for the WPT system depicted in Fig. 1, the topology and nominal component parameters are known. Benefiting from this, the model order can be determined using the conventional method along with some model order reduction techniques, and then, the associated model parameters are accurately estimated using the data-driven method. The idea of using parameterized models was also considered in [34].

Pure time delays are a common feature of WPT systems, which can occur, for example, when the control signals pass the optocouplers, when the MOSFETs are switched ON or OFF, or when the measured output is sent to the host computer via wireless communication. Therefore, to provide an approximate but accurate description of the system input–output behavior, the structure of linear rational model plus pure time delay has been widely adopted, even though this model structure will complicate the parameter estimation process due to the time delay,

which is a nonlinear parameter in the model. Note that, in dealing with the model estimation scenarios where the time delay is a fraction of the sample time, continuous-time (CT) models are a natural choice [7], [16], [17]. By contrast, in discrete-time (DT) models, the time delay is always set to an integer number of the sample time, in order to facilitate the digital simulation. Without loss of generality, the estimation method will be developed initially in the CT context and, afterwards, extended to handle DT model estimation.

A few data-driven CT modeling approaches have been proposed in the literature to estimate both the rational model parameters and time delay of a CT model, such as the prediction error method [25], the instrumental variable (IV) method [7], [35], and the linear least-squares (LS) method [1]. The main benefit of IV methods lies in that they provide a simple LS-like solution, but the resulting parameter estimates can be consistent even in the presence of measurement noise [30], [36]. The refined IV (RIV) method is one of the most reliable implementations of IV estimators, which was first proposed by Young and Jakeman initially for DT models [38] and later extended for CT models. On the other hand, the simplified RIV for CT models (SRIVC) method has been extended to estimate the parameters of a time-delay CT model [3], [7], where *simplified* means that the measurement noise is assumed to be white. The developed method operates in an iterative and separable manner, combining an IV method for the rational model parameters with an adaptive search for the time delay.

In practical applications, control design is usually based on CT models, while in digital implementation, either CT or DT models can be used [12], [41]. In view of this background, it could be more beneficial if a method can handle both CT and DT model estimation. To achieve this, an option is to derive a frequency-domain version of the method in [7] following from the idea of [19]. The frequency-domain method is able to estimate both CT and DT models uniformly, compared to its time-domain version in [7] that is dedicated to CT models only. It is worth mentioning that the new method is very suited to embedded applications, since many advanced microprocessors have built-in hardware to help implement the fast Fourier transform (FFT). As another advantage, the frequency-domain method has no need to round the time delay to an integer number of the sample time even in the DT modeling scenario, thanks to the use of frequency variables that are free from shift operations. However, this merit is lost for some gradient-based time-domain approaches relying on shift operators, where a rounding operation is required at each iteration, and this inevitably limits the convergence performance.

The remainder of this paper is organized as follows. The analytical modeling method is recalled in Section II. The proposed data-driven modeling method is derived in Section III. Numerical and experimental results are presented in Sections IV and V. Finally, conclusions are drawn in Section VI.

II. Analytical Modeling

For the circuit diagram depicted in Fig. 1, there are totally five reactive components: four in the resonant tank and one in the output filter, indicating that the circuit can be characterized by five equations. To find out these, the following assumptions are made, and further explanations are given in Remark 1.

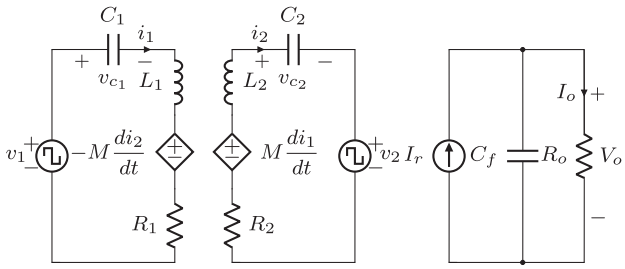

Fig. 3. First harmonic equivalent of the circuit in Fig. 1.

Assumption 1:

1) The switches and diodes are ideal components, that is, all parasitic resistances, inductances, and capacitances, and forward voltages are zero.
2) The switching frequency ω_s is fixed, the phase shift α is a constant, and the dead band γ is zero.
3) Both the sending and receiving resonators are at or sufficiently close to the resonant state.

Remark 1: The first assumption is imposed to facilitate the derivation of model (1) without considering power losses. The second assumption is imposed to ensure that both v_1 and v_2 are periodic, so that the system is only excited at discrete frequency points $\{k\omega_s | k \in \mathbb{Z}\}$ when all transients have died out. The last assumption allows only the first harmonic to pass through the resonant tank, while the other high-order terms are blocked. The second and third assumptions together guarantee the accuracy of the first harmonic approximation in (2), (3), (5), and (7).

Under Assumption 1, the original circuit can be simplified to the one sketched in Fig. 3 by using the method presented in [12], [13], and [41], where the dc source and the inverter are represented by the ac voltage source v_1, and the influence of the coupling inductors is replaced by two current-dependent voltage sources [11]. Subsequently, by using the current of inductors and the voltage of capacitors as variables, according to Kirchoff's voltage law, the following equations are established to describe the circuit behavior:

$$L_1\frac{di_1}{dt} = v_1 - v_{c_1} + M\frac{di_2}{dt} - i_1R_1 \tag{1a}$$

$$L_2\frac{di_2}{dt} = M\frac{di_1}{dt} - v_{c_2} - v_2 - i_2R_2 \tag{1b}$$

$$C_1\frac{dv_{c_1}}{dt} = i_1 \tag{1c}$$

$$C_2\frac{dv_{c_2}}{dt} = i_2 \tag{1d}$$

$$C_f\frac{dV_o}{dt} = I_r - \frac{V_o}{R_o}. \tag{1e}$$

In (1), the first four ac equations correspond to the resonant tank, whereas the last dc equation corresponds to the output filter. Needless to say, mixing ac and dc signals complicates the theoretical analysis for sure, and as a consequence, all equations should be converted into pure dc ones. A variety of techniques

have been proposed to eliminate the ac signals and establish the large- and small-signal models, e.g., state-space averaging [23], [33] and harmonic approximation [39], [41]. In this paper, just as an example, the harmonic approximation technique is adopted.

A. Large-Signal Model

The WPT system depicted in Fig. 1 is, in nature, a resonant converter, which is highly frequency selective. Therefore, when the second and third points of Assumption 1 are fulfilled, only the fundamental of v_1 can pass through the resonant tank, while the other high-order terms are blocked. From this point of view, the ac signals in the resonant tank can be approximated by their first harmonic without leading to a substantial loss in the accuracy. Bearing this in mind and according to [12] and [41], a signal in the resonant tank can be decomposed as a sum of d-axis and q-axis components, e.g.,

$$v_1 \approx V_{1d}\sin(\omega_s t) + V_{1q}\cos(\omega_s t) \tag{2a}$$

$$i_1 \approx I_{1d}\sin(\omega_s t) + I_{1q}\cos(\omega_s t) \tag{2b}$$

where capital letters stand for the amplitude of a signal. The ac signals in the receiving resonator can be decomposed along the same line. Note that the sources v_1, v_2, and I_r are nonlinear in the variables, and in what follows, further details to obtain the analytical expressions are presented.

1) v_1 can be expressed as $v_1 = v_a - v_b$, where v_a and v_b denote, respectively, the voltages at points A and B in Fig. 1. It can be shown that both v_a and v_b are square waves with amplitude switching between 0 and V_d, where V_d the voltage of the dc source. Compared to v_a, v_b has a phase lag of $-\pi-\alpha$, where α is the phase shift between the leading and lagging legs specified by the experimenter. Assuming that the phases of v_a and v_b are, respectively, $\alpha/2$ and $-\pi-\alpha/2$, the first harmonic approximation of v_1 is given as

$$\begin{aligned} v_1 &= v_a - v_b \\ &\approx \frac{2V_d}{\pi}\left(\sin\left(\omega_s t + \frac{\alpha}{2}\right) - \sin\left(\omega_s t - \pi - \frac{\alpha}{2}\right)\right) \\ &= \frac{4V_d}{\pi}\cos\left(\frac{\alpha}{2}\right)\sin(\omega_s t) \end{aligned} \tag{3}$$

showing that

$$V_{1d} = \frac{4V_d}{\pi}\cos\left(\frac{\alpha}{2}\right), \quad V_{1q} = 0. \tag{4}$$

2) Due to the clamping effect of the rectifier bridge, v_2 is a square wave with amplitude switching between $\pm V_o$ and has the same sign than i_2, i.e., $v_2 = \mathrm{sgn}(i_2)V_o$. This phenomenon is evidenced from the bottom plot of Fig. 2. Meanwhile, since i_2 is very close to a sinusoid of frequency ω_s, the first harmonic approximation of v_2 can be defined in terms of i_2 as follows:

$$\begin{aligned} v_2 = \mathrm{sgn}(i_2)V_o &\approx \frac{4V_o}{\pi}\frac{i_2}{\|i_2\|} \\ &= \frac{4V_o}{\pi}\frac{1}{\|i_2\|}\left(I_{2d}\sin(\omega_s t) + I_{2q}\cos(\omega_s t)\right) \end{aligned} \tag{5}$$

where $\|i_2\| = \sqrt{I_{2d}^2 + I_{2q}^2}$. It is then clear that

$$[V_{2d}, V_{2q}] = \frac{4V_o}{\pi\sqrt{I_{2d}^2 + I_{2q}^2}}[I_{2d}, I_{2q}]. \tag{6}$$

3) When the rectifiers are considered as ideal components, according to the law of energy conservation, I_r is equal to the mean value of $|i_2|$. Letting $T_s = 2\pi/\omega_s$, we have

$$\begin{aligned} I_r &= \frac{1}{T_s}\int_0^{T_s}|i_2|dt = \frac{\|i_2\|}{T_s}\int_0^{T_s}|\sin(\omega_s t)|dt \\ &= \frac{2}{\pi}\sqrt{I_{2d}^2 + I_{2q}^2}. \end{aligned} \tag{7}$$

Subsequently, by substituting (2)–(7) into (1), the d- and q-components are separated as follows:

$$\begin{aligned} \frac{dI_{1d}}{dt} &= \omega_s I_{1q} + \Upsilon_1(V_{1d} - V_{c_1 d} - I_{1d}R_1) \\ &\quad - \Upsilon_2(\Upsilon_4 I_{2d} + V_{c_2 d} + I_{2d}R_2) \end{aligned} \tag{8a}$$

$$\begin{aligned} \frac{dI_{2d}}{dt} &= \omega_s I_{2q} + \Upsilon_2(V_{1d} - V_{c_1 d} - I_{1d}R_1) \\ &\quad - \Upsilon_3(\Upsilon_4 I_{2d} + V_{c_2 d} + I_{2d}R_2) \end{aligned} \tag{8b}$$

$$\frac{dV_{c_1 d}}{dt} = \omega_s V_{c_1 q} + \frac{1}{C_1}I_{1d} \tag{8c}$$

$$\frac{dV_{c_2 d}}{dt} = \omega_s V_{c_2 q} + \frac{1}{C_2}I_{2d} \tag{8d}$$

$$\begin{aligned} \frac{dI_{1q}}{dt} &= -\omega_s I_{1d} - \Upsilon_1(V_{c_1 q} + I_{1q}R_1) \\ &\quad - \Upsilon_2(\Upsilon_4 I_{2q} + V_{c_2 q} + I_{2q}R_2) \end{aligned} \tag{8e}$$

$$\begin{aligned} \frac{dI_{2q}}{dt} &= -\omega_s I_{2d} - \Upsilon_2(V_{c_1 q} + I_{1q}R_1) \\ &\quad - \Upsilon_3(\Upsilon_4 I_{2q} + V_{c_2 q} + I_{2q}R_2) \end{aligned} \tag{8f}$$

$$\frac{dV_{c_1 q}}{dt} = -\omega_s V_{c_1 d} + \frac{1}{C_1}I_{1q} \tag{8g}$$

$$\frac{dV_{c_2 q}}{dt} = -\omega_s V_{c_2 d} + \frac{1}{C_2}I_{2q} \tag{8h}$$

$$\frac{dV_o}{dt} = \frac{1}{C_f}\left(I_r - \frac{V_o}{R_o}\right) \tag{8i}$$

where

$$[\Upsilon_1, \Upsilon_2, \Upsilon_3] = \frac{1}{L_1 L_2 - M^2}[L_2, M, L_1] \tag{9a}$$

$$\Upsilon_4 = \frac{4V_o}{\pi\sqrt{I_{2d}^2 + I_{2q}^2}}. \tag{9b}$$

The set of equations in (8) is the so-called large-signal model, which can be written in the equivalent state-space form as

$$\begin{cases} \dfrac{d\boldsymbol{X}(t)}{dt} = \boldsymbol{A}\boldsymbol{X}(t) + \boldsymbol{B} \\ V_o(t) = \boldsymbol{C}\boldsymbol{X}(t) \end{cases} \tag{10}$$

where $\{\boldsymbol{A}, \boldsymbol{B}, \boldsymbol{C}\}$ and $\boldsymbol{X}(t)$ are defined in (11) shown at the bottom of this page.

Remark 2: The dq decomposition has the deficiency of increasing the model order: the original dynamic model (1) is of order 5, but the resulting large-signal model (10) is of order 9. There exist some modeling methods free from this problem, e.g., the coupled mode-based method [23]. However, even if they are applied to the system in Fig. 1, the resulting model is of order 5, which is still very high for control design. Therefore, model reduction is always necessary for all these methods to yield a desired low-order model.

B. Small-Signal Model

Due to the nonlinear relationship between V_{1d} and α [see (4)], the large-signal model (10) cannot be written in input–output form necessary for control design. Therefore, the large-signal model needs to be linearized around some static point to obtain a small-signal model that is linear in the variables. To this end, all the signals in the circuit should be decomposed as a static value plus a small signal, e.g., $V_o = \overline{V}_o + \tilde{v}_o$, where $\overline{V}_o$ and $\tilde{v}_o$ denote the static and small-signal parts, respectively. Note that the decomposition of V_{1d}, V_{2d}, V_{2q}, and I_r should be carefully handled, since they are nonlinear in the variables. Here, the first-order Taylor expansion is used, which yields the following expressions:

$$\tilde{v}_{1d} \approx -\Upsilon_{11}\tilde{\alpha} \tag{13a}$$

$$\tilde{v}_{2d} \approx (\Upsilon_{10} - \Upsilon_5)\tilde{i}_{2d} - \Upsilon_6\tilde{i}_{2q} + \Upsilon_8\tilde{v}_o \tag{13b}$$

$$\tilde{v}_{2q} \approx (\Upsilon_{10} - \Upsilon_7)\tilde{i}_{2q} - \Upsilon_6\tilde{i}_{2d} + \Upsilon_9\tilde{v}_o \tag{13c}$$

$$\tilde{i}_r \approx \frac{1}{2}\left(\Upsilon_8\tilde{i}_{2d} + \Upsilon_9\tilde{i}_{2q}\right) \tag{13d}$$

where

$$[\Upsilon_5, \Upsilon_6, \Upsilon_7] = \frac{4\overline{V}_o}{\pi\sqrt{\left(\overline{I}_{2d}^2 + \overline{I}_{2q}^2\right)^3}}\left[\overline{I}_{2d}^2, \overline{I}_{2d}\overline{I}_{2q}, \overline{I}_{2q}^2\right] \tag{14a}$$

$$[\Upsilon_8, \Upsilon_9, \Upsilon_{10}] = \frac{4}{\pi\sqrt{\overline{I}_{2d}^2 + \overline{I}_{2q}^2}}\left[\overline{I}_{2d}, \overline{I}_{2q}, \overline{V}_o\right] \tag{14b}$$

$$\Upsilon_{11} = \frac{2V_d}{\pi}\sin\left(\frac{\overline{\alpha}}{2}\right). \tag{14c}$$

$$\boldsymbol{A} = \begin{bmatrix} -\Upsilon_1 R_1 & -\Upsilon_2(\Upsilon_4 + R_2) & -\Upsilon_1 & -\Upsilon_2 & \omega_s & 0 & 0 & 0 & 0 \\ -\Upsilon_2 R_1 & -\Upsilon_3(\Upsilon_4 + R_2) & -\Upsilon_2 & -\Upsilon_3 & 0 & \omega_s & 0 & 0 & 0 \\ 1/C_1 & 0 & 0 & 0 & 0 & 0 & \omega_s & 0 & 0 \\ 0 & 1/C_2 & 0 & 0 & 0 & 0 & 0 & \omega_s & 0 \\ -\omega_s & 0 & 0 & 0 & -\Upsilon_1 R_1 & -\Upsilon_2(\Upsilon_4 + R_2) & -\Upsilon_1 & -\Upsilon_2 & 0 \\ 0 & -\omega_s & 0 & 0 & -\Upsilon_2 R_1 & -\Upsilon_3(\Upsilon_4 + R_2) & -\Upsilon_2 & -\Upsilon_3 & 0 \\ 0 & 0 & -\omega_s & 0 & 1/C_1 & 0 & 0 & 0 & 0 \\ 0 & 0 & 0 & -\omega_s & 0 & 1/C_2 & 0 & 0 & 0 \\ 0 & 0 & 0 & 0 & 0 & 0 & 0 & 0 & -1/(C_f R_o) \end{bmatrix} \tag{11a}$$

$$\boldsymbol{B} = \left[\Upsilon_1 V_{1d}, \Upsilon_2 V_{1d}, 0, 0, 0, 0, 0, 0, I_r/C_f\right]^\top \tag{11b}$$

$$\boldsymbol{C} = \left[0, 0, 0, 0, 0, 0, 0, 0, 1\right] \tag{11c}$$

$$\boldsymbol{X}(t) = \left[I_{1d}(t), I_{2d}(t), V_{c_1 d}(t), V_{c_2 d}(t), I_{1q}(t), I_{2q}(t), V_{c_1 q}(t), V_{c_2 q}(t), V_o(t)\right]^\top \tag{11d}$$

$$\boldsymbol{F} = \begin{bmatrix} -\Upsilon_1 R_1 & -\Upsilon_2(\Upsilon_{10} + R_2 - \Upsilon_5) & -\Upsilon_1 & -\Upsilon_2 & \omega_s & \Upsilon_2\Upsilon_6 & 0 & 0 & -\Upsilon_2\Upsilon_8 \\ -\Upsilon_2 R_1 & -\Upsilon_3(\Upsilon_{10} + R_2 - \Upsilon_5) & -\Upsilon_2 & -\Upsilon_3 & 0 & \omega_s + \Upsilon_3\Upsilon_6 & 0 & 0 & -\Upsilon_3\Upsilon_8 \\ 1/C_1 & 0 & 0 & 0 & 0 & 0 & \omega_s & 0 & 0 \\ 0 & 1/C_2 & 0 & 0 & 0 & 0 & 0 & \omega_s & 0 \\ -\omega_s & \Upsilon_2\Upsilon_6 & 0 & 0 & -\Upsilon_1 R_1 & -\Upsilon_2(\Upsilon_{10} + R_2 - \Upsilon_7) & -\Upsilon_1 & -\Upsilon_2 & -\Upsilon_2\Upsilon_9 \\ 0 & -\omega_s + \Upsilon_3\Upsilon_6 & 0 & 0 & -\Upsilon_2 R_1 & -\Upsilon_3(\Upsilon_{10} + R_2 - \Upsilon_7) & -\Upsilon_2 & -\Upsilon_3 & -\Upsilon_3\Upsilon_9 \\ 0 & 0 & -\omega_s & 0 & 1/C_1 & 0 & 0 & 0 & 0 \\ 0 & 0 & 0 & -\omega_s & 0 & 1/C_2 & 0 & 0 & 0 \\ 0 & \Upsilon_8/(2C_f) & 0 & 0 & 0 & \Upsilon_9/(2C_f) & 0 & 0 & -1/(C_f R_o) \end{bmatrix} \tag{12a}$$

$$\boldsymbol{G} = \left[-\Upsilon_1\Upsilon_{11}, -\Upsilon_2\Upsilon_{11}, 0, 0, 0, 0, 0, 0, 0\right]^\top \tag{12b}$$

$$\boldsymbol{H} = \left[0, 0, 0, 0, 0, 0, 0, 0, 1\right] \tag{12c}$$

$$\tilde{\boldsymbol{x}}(t) = \left[\tilde{i}_{1d}(t), \tilde{i}_{2d}(t), \tilde{v}_{c_1 d}(t), \tilde{v}_{c_2 d}(t), \tilde{i}_{1q}(t), \tilde{i}_{2q}(t), \tilde{v}_{c_1 q}(t), \tilde{v}_{c_2 q}(t), \tilde{v}_o(t)\right]^\top \tag{12d}$$

By subtracting the static parts in (8) and similar to (10), the small-signal model in state-space form is obtained as

$$\begin{cases} \dfrac{d\tilde{\boldsymbol{x}}(t)}{dt} = \boldsymbol{F}\tilde{\boldsymbol{x}}(t) + \boldsymbol{G}\tilde{\alpha}(t) \\ \tilde{v}_o(t) = \boldsymbol{H}\tilde{\boldsymbol{x}}(t) \end{cases} \tag{15}$$

where $\{\boldsymbol{F}, \boldsymbol{G}, \boldsymbol{H}\}$ and $\tilde{\boldsymbol{x}}(t)$ are defined in (12) shown at the bottom of the previous page.

Remark 3: The analytical modeling method has some merits: thanks to the use of physical laws that are known to govern the behavior of the system, the resulting model is reliable, and the associated model parameters provide physical insights into the system. However, it has also several shortcomings. First, it requires to know the true parameters of circuit components, which can be hard in industrial practice. Second, the resulting model is of high order (order 9), which is not suited to control design. Some reduction techniques have been available to reduce the model order (see Section IV), but they inevitably deteriorate the model accuracy. Finally, it is not possible to estimate the time delay. As a remedy to the above-mentioned shortcomings, the data-driven modeling method is proposed in the next section to refine the model quality.

III. Data-Driven Modeling

For brevity of exposition, the phase shift $\tilde{\alpha}$ and the output voltage $\tilde{v}_o$ defined in the previous section will be replaced by u and y, respectively. Based on these, the system input–output behavior is described by the so-called output-error model

$$\begin{cases} x(t) = G(s, \boldsymbol{\theta})u(t-\tau) = \dfrac{B(s, \boldsymbol{\theta})}{A(s, \boldsymbol{\theta})}u(t-\tau) \\ y(t_k) = x(t_k) + e(t_k) \end{cases} \tag{16}$$

where s is the Laplace operator, $\tau \geqslant 0$ is the pure time delay, and $\{e(t_k)\}$ is a DT white noise sequence. It is assumed that the input–output signals are regularly sampled at time instant $t_k = kT$, $k \in \mathbb{N}^+$, where T is the sample time. Polynomials $B(s, \boldsymbol{\theta})$ and $A(s, \boldsymbol{\theta})$ take the forms

$$B(s, \boldsymbol{\theta}) = b_0 s^{n_b} + \cdots + b_{n_b} \tag{17a}$$

$$A(s, \boldsymbol{\theta}) = s^{n_a} + a_1 s^{n_a - 1} + \cdots + a_{n_a},\ n_a \geqslant n_b. \tag{17b}$$

It is further assumed that $B(s, \boldsymbol{\theta})$ and $A(s, \boldsymbol{\theta})$ are coprime, and that the roots of $A(s, \boldsymbol{\theta})$ are located on the left-half plane. The unknown rational model parameters are stacked in a vector

$$\boldsymbol{\theta} = [a_1, \ldots, a_{n_a}, b_0, \ldots, b_{n_b}]^\top \in \mathbb{R}^{n_a + n_b + 1}. \tag{18}$$

Then, provided that the polynomial degrees n_a and n_b have been determined by the analytical modeling method in Section II, the objective is to estimate the unknown parameter vector $\boldsymbol{\theta}$ and the time delay τ from the sampled input–output data $\{y(t_k), u(t_k)\}_{k=1}^N$.

Remark 4: This paper aims at solving the estimation problem in the frequency domain. Thus, in the first step, one needs to recover the frequency-domain data from the time-domain counterpart. As illustrated in [27] and [29], the frequency measurements are mostly done by using the discrete Fourier transform (DFT), which calculates the spectrum on a discrete equidistant set of frequencies. It is strongly recommended to apply a periodic input signal and then sample the input–output signals over an integer number of periods. In this case, the DFT spectrum will give an exact copy of the original spectrum. Otherwise, the signal at one frequency line will leak into the neighboring frequency lines, which is called leakage. Besides, the input signal for data-driven modeling should be sufficiently rich in harmonics to ensure that the true system parameters are identifiable [4], [7].

Applying DFT to the sampled input data, normally implemented as the FFT algorithm, yields

$$U(\omega_k) = T\sum_{\ell=1}^{N} u(t_\ell)\mathrm{e}^{-i\omega_k t_\ell} \tag{19}$$

where $\omega_k = 2\pi k/(NT)$. The output spectrum $Y(\omega_k)$ and the residual spectrum $E(\omega_k)$ can be similarly defined. Subsequently, letting $s = i\omega_k$, model (16) has the following frequency-domain formulation:

$$Y(\omega_k) = G(i\omega_k, \boldsymbol{\theta})\mathrm{e}^{-i\omega_k\tau}U(\omega_k) + E(\omega_k). \tag{20}$$

When degrees n_a and n_b have been determined by the analytical modeling method in Section II, the parameter estimation problem is to estimate the vector $\boldsymbol{\theta}$ and the time delay τ by minimizing the following output-error loss function:

$$\hat{\boldsymbol{\theta}}, \hat{\tau} = \arg\min_{\boldsymbol{\theta}, \tau} J(\boldsymbol{\theta}, \tau) \tag{21a}$$

$$J(\boldsymbol{\theta}, \tau) = \frac{1}{2N}\sum_{k=1}^{N} \|\Xi(\omega_k, \boldsymbol{\theta}, \tau)\|_2^2 \tag{21b}$$

where

$$\Xi(\omega_k, \boldsymbol{\theta}, \tau) = Y(\omega_k) - G(i\omega_k, \boldsymbol{\theta})\mathrm{e}^{-i\omega_k\tau}U(\omega_k) \tag{22}$$

is the output error. A variety of methods have been proposed in the literature to solve the above optimization problem, e.g., the LS methods, the IV methods, the prediction error methods (see, e.g., [24]), and the subspace-based methods. In this paper, the IV method will be used, with particular reference to the SRIVC method, which has already been extended in [7] to handle the time-delay CT system identification problem in the time domain. The method developed therein is an iterative and separable procedure. More specifically, at each iteration, it consists of an IV method to estimate $\boldsymbol{\theta}$ by fixing τ, followed by a one-dimensional numerical search to solve for τ by letting $\boldsymbol{\theta}$ as a function of τ. This method is a direct extension of the conventional SRIVC method to estimate both the plant parameters and the time delay of a model with only a slight increase in the algorithmic complexity. In the following sections, the frequency-domain version of the method in [7] will be developed to optimize (21).

A. Plant Model Parameter Estimation

The estimation of $\boldsymbol{\theta}$ by fixing τ is considered in this subsection. Similar to the time-domain SRIVC method, the output error

defined in (22) is decomposed as

$$\begin{aligned}\Xi(\omega_k,\boldsymbol{\theta},\tau)&=Y(\omega_k)-G(i\omega_k,\boldsymbol{\theta})\mathrm{e}^{-i\omega_k\tau}U(\omega_k)\\&=\frac{1}{A(i\omega_k,\boldsymbol{\theta})}\big(A(i\omega_k,\boldsymbol{\theta})Y(\omega_k)-B(i\omega_k,\boldsymbol{\theta})\mathrm{e}^{-i\omega_k\tau}U(\omega_k)\big)\\&=A(i\omega_k,\boldsymbol{\theta})Y_F(\omega_k)-B(i\omega_k,\boldsymbol{\theta})\mathrm{e}^{-i\omega_k\tau}U_F(\omega_k)\end{aligned}\tag{23}$$

where the subscript $(\cdot)_F$ means that the associated variable has been filtered by $F(i\omega_k,\boldsymbol{\theta})=1/A(i\omega_k,\boldsymbol{\theta})$. Note that this filtering operation cannot be directly implemented, since it depends on $\boldsymbol{\theta}$, which is *a priori* unknown. To solve this problem, an iterative algorithm is adopted for practical implementation: at the $(r+1)$th iteration, the value of $\boldsymbol{\theta}$ is set to its latest estimate obtained at the previous iteration $\hat{\boldsymbol{\theta}}^r$. Then, the filtered input–output signals are computed as follows:

$$Y_F(\omega_k)=F(i\omega_k,\hat{\boldsymbol{\theta}}^r)Y(\omega_k)=\frac{1}{A(i\omega_k,\hat{\boldsymbol{\theta}}^r)}Y(\omega_k)\tag{24a}$$

$$U_F(\omega_k)=F(i\omega_k,\hat{\boldsymbol{\theta}}^r)U(\omega_k)=\frac{1}{A(i\omega_k,\hat{\boldsymbol{\theta}}^r)}U(\omega_k).\tag{24b}$$

Subsequently, (23) can be written into the so-called pseudo-linear regression form (see [36]) in terms of the above filtered input–output signals

$$\Xi(\omega_k,\boldsymbol{\theta},\tau)=\tilde{Y}_F(\omega_k)-\boldsymbol{\Phi}_F^\top(\omega_k,\tau)\boldsymbol{\theta}\tag{25}$$

where

$$\tilde{Y}_F(\omega_k)=(i\omega_k)^{n_a}Y_F(\omega_k)\tag{26}$$

and $\boldsymbol{\Phi}_F(\omega_k,\tau)\in\mathbb{C}^{n_a+n_b+1}$ is the filtered regression vector

$$\begin{aligned}\boldsymbol{\Phi}_F^\top(\omega_k,\tau)=\big[&-[(i\omega_k)^{n_a-1},\ldots,1]Y_F(\omega_k),\\&[(i\omega_k)^{n_b},\ldots,1]\mathrm{e}^{-i\omega_k\tau}U_F(\omega_k)\big].\end{aligned}\tag{27}$$

It can be seen that (25) is now linear in $\boldsymbol{\theta}$, enabling the LS method to estimate $\boldsymbol{\theta}$. However, as $\boldsymbol{\Phi}_F(\omega_k,\tau)$ is correlated with the measurement noise $E(\omega_k)$, the resulting LS estimate will be biased, even if the noise is purely white. In order to eliminate the bias, the IV technique is adopted. The IV estimate of $\boldsymbol{\theta}$ as a function of τ, say $\hat{\boldsymbol{\theta}}(\tau)$, is the solution to the following problem:

$$\hat{\boldsymbol{\theta}}(\tau)=\arg\min_{\boldsymbol{\theta}}\left\|\frac{1}{N}\sum_{k=1}^{N}\hat{\boldsymbol{\Phi}}_F(\omega_k)\Xi(\omega_k,\boldsymbol{\theta},\tau)\right\|_2^2\tag{28}$$

where $\hat{\boldsymbol{\Phi}}_F(\omega_k)\in\mathbb{C}^{n_a+n_b+1}$ is a user-specified instrument uncorrelated with $E(\omega_k)$ but maximally correlated with $\boldsymbol{\Phi}_F(\omega_k,\tau)$. In the SRIVC case, the following choice is used:

$$\begin{aligned}\hat{\boldsymbol{\Phi}}_F^\top(\omega_k)=\Big[&-[(i\omega_k)^{n_a-1},\ldots,1]\hat{Y}_F(\omega_k),\\&[(i\omega_k)^{n_b},\ldots,1]\mathrm{e}^{-i\omega_k\hat{\tau}^r}U_F(\omega_k)\Big]\end{aligned}\tag{29}$$

where $\hat{Y}_F(\omega_k)$ is the noise-free version of $Y_F(\omega_k)$ computed by using the model built from the latest estimates $\hat{\boldsymbol{\theta}}^r$ and $\hat{\tau}^r$

$$\hat{Y}_F(\omega_k)=G(i\omega_k,\hat{\boldsymbol{\theta}}^r)\mathrm{e}^{-i\omega_k\hat{\tau}^r}U_F(\omega_k).\tag{30}$$

Finally, by substituting (25) into (28), $\boldsymbol{\theta}$ is estimated as

$$\hat{\boldsymbol{\theta}}(\tau)=\left(\sum_{k=1}^{N}\hat{\boldsymbol{\Phi}}_F(\omega_k)\boldsymbol{\Phi}_F^\top(\omega_k,\tau)\right)^{-1}\sum_{k=1}^{N}\hat{\boldsymbol{\Phi}}_F(\omega_k)\tilde{Y}_F(\omega_k).\tag{31}$$

B. Time-Delay Estimation

By substituting the obtained $\hat{\boldsymbol{\theta}}(\tau)$ in (31) into the original loss function (21), the optimization problem reduces to

$$\hat{\tau}=\arg\min_{\tau}\breve{J}(\tau)\tag{32a}$$

$$\breve{J}(\tau)=J(\boldsymbol{\theta},\tau)|_{\boldsymbol{\theta}=\hat{\boldsymbol{\theta}}(\tau)}.\tag{32b}$$

Since $\breve{J}(\tau)$ is nonlinear in τ, the optimization is solved via numerical search, with the solution given as

$$\hat{\tau}^{r+1}=\hat{\tau}^r-\mu^r\left(\nabla^2\breve{J}(\hat{\tau}^r)\right)^{-1}\nabla\breve{J}(\hat{\tau}^r)\tag{33}$$

where μ^r is a scaling factor that defines the step length. $\nabla^2\breve{J}(\hat{\tau}^r)$ and $\nabla\breve{J}(\hat{\tau}^r)$ are the Hessian matrix and gradient vector of $\breve{J}(\tau)$ evaluated at $\hat{\tau}^r$, respectively. In what follows, further details on how to compute the two terms are presented. Before this, the IV formulation of (32a) is established similar to (28) as

$$\hat{\tau}=\arg\min_{\tau}\left\|\frac{1}{N}\sum_{k=1}^{N}\hat{\Psi}(\omega_k)\breve{\Xi}(\omega_k,\tau)\right\|_2^2\tag{34}$$

where $\hat{\Psi}(\omega_k)\in\mathbb{C}$ is the instrument and

$$\begin{aligned}\breve{\Xi}(\omega_k,\tau)&=\Xi(\omega_k,\boldsymbol{\theta},\tau)|_{\boldsymbol{\theta}=\hat{\boldsymbol{\theta}}(\tau)}\\&=\tilde{Y}_F(\omega_k)-\boldsymbol{\Phi}_F^\top(\omega_k,\tau)\hat{\boldsymbol{\theta}}(\tau).\end{aligned}\tag{35}$$

Note that the instrument $\hat{\boldsymbol{\Phi}}_F^\top(\omega_k)$ in (29) can be written as

$$\begin{aligned}\hat{\boldsymbol{\Phi}}_F^\top(\omega_k)&=\frac{1}{A(i\omega_k,\hat{\boldsymbol{\theta}}^r)}\Big[-[(i\omega_k)^{n_a-1},\ldots,1]G(i\omega_k,\hat{\boldsymbol{\theta}}^r),\\&\qquad[(i\omega_k)^{n_b},\ldots,1]\Big]\mathrm{e}^{-i\omega_k\hat{\tau}^r}U(\omega_k)\\&=\left[\frac{\partial G(i\omega_k,\boldsymbol{\theta})}{\partial a_1},\ldots,\frac{\partial G(i\omega_k,\boldsymbol{\theta})}{\partial b_{n_b}}\right]\\&\quad\times\mathrm{e}^{-i\omega_k\tau}U(\omega_k)\big|_{\boldsymbol{\theta}=\hat{\boldsymbol{\theta}}^r,\tau=\hat{\tau}^r}\\&=-\frac{\partial\Xi(\omega_k,\boldsymbol{\theta},\tau)}{\partial\boldsymbol{\theta}}\bigg|_{\boldsymbol{\theta}=\hat{\boldsymbol{\theta}}^r,\tau=\hat{\tau}^r}\end{aligned}\tag{36}$$

which is, in fact, the minus one partial derivative of $\Xi(\omega_k,\boldsymbol{\theta},\tau)$ in (22) with respect to $\boldsymbol{\theta}$ evaluated at $(\hat{\boldsymbol{\theta}}^r,\hat{\tau}^r)$. Inspired by the above relation, $\hat{\Psi}(\omega_k)$ can be constructed along a similar line. Differentiating on both sides of (22) with respect to τ gives

$$\begin{aligned}\hat{\Psi}^\top(\omega_k)&=-\frac{\partial\Xi(\omega_k,\boldsymbol{\theta},\tau)}{\partial\tau}\bigg|_{\boldsymbol{\theta}=\hat{\boldsymbol{\theta}}^r,\tau=\hat{\tau}^r}\\&=G(i\omega_k,\boldsymbol{\theta})U(\omega_k)\frac{d\mathrm{e}^{-i\omega_k\tau}}{d\tau}\bigg|_{\boldsymbol{\theta}=\hat{\boldsymbol{\theta}}^r,\tau=\hat{\tau}^r}\\&=-i\omega_kG(i\omega_k,\hat{\boldsymbol{\theta}}^r)\mathrm{e}^{-i\omega_k\hat{\tau}^r}U(\omega_k).\end{aligned}\tag{37}$$

Then, $\nabla^2\breve{J}(\tau)$ and $\nabla\breve{J}(\tau)$ are approximated as

$$\nabla\breve{J}(\tau) = -\frac{1}{N}\sum_{k=1}^{N}\hat{\Psi}(\omega_k)\breve{\Xi}(\omega_k,\tau) \tag{38a}$$

$$\begin{aligned}\nabla^2\breve{J}(\tau) &= -\frac{1}{N}\sum_{k=1}^{N}\hat{\Psi}(\omega_k)\frac{d\breve{\Xi}(\omega_k,\tau)}{d\tau}\\ &= \frac{1}{N}\sum_{k=1}^{N}\hat{\Psi}(\omega_k)\left(\frac{d\boldsymbol{\Phi}_F^\top(\omega_k,\tau)}{d\tau}\hat{\boldsymbol{\theta}}(\tau)\right.\\ &\quad\left.+\boldsymbol{\Phi}_F^\top(\omega_k,\tau)\frac{d\hat{\boldsymbol{\theta}}(\tau)}{d\tau}\right)\\ &= \frac{1}{N}\sum_{k=1}^{N}\hat{\Psi}(\omega_k)\,\Psi^\top(\omega_k,\tau)\\ &\quad-\frac{1}{N}\sum_{k=1}^{N}\hat{\Psi}(\omega_k)\boldsymbol{\Phi}_F^\top(\omega_k,\tau)\\ &\quad\times\left(\sum_{k=1}^{N}\hat{\boldsymbol{\Phi}}_F(\omega_k)\boldsymbol{\Phi}_F^\top(\omega_k,\tau)\right)^{-1}\\ &\quad\times\sum_{k=1}^{N}\hat{\boldsymbol{\Phi}}_F(\omega_k)\,\Psi^\top(\omega_k,\tau)\end{aligned} \tag{38b}$$

where

$$\Psi^\top(\omega_k,\tau) = \frac{d\boldsymbol{\Phi}_F^\top(\omega_k,\tau)}{d\tau}\hat{\boldsymbol{\theta}}(\tau). \tag{39}$$

C. Generating Initial Values

Since the proposed method is an iterative procedure to approach the optimal estimate starting from some initial guess, the choice of initial values is an important issue. The initial value for $\boldsymbol{\theta}$ can be generated by using the standard LS-based state variable filter (see, e.g., [15]) method with τ set to its initial value. On the other hand, the loss function is usually a nonlinear function with respect to τ, and thus, the gradient-based search (33) to estimate τ may be trapped by local minima. To increase the chance of converging to the global optimum, it is suggested to provide a grid for τ and select the best as the initial value based on the chosen criteria. The above procedure to generate initial values for $\boldsymbol{\theta}$ and τ is summarized in Algorithm 1. Similar to [5], some guidelines regarding the selection of the hyperparameters in the algorithm are given as follows.

1) *Choice of $\overline{\tau}$ and $\underline{\tau}$:* The lower time-delay boundary $\underline{\tau}$ can always be set to zero, while $\overline{\tau}$ can be obtained by maximizing the following cross-correlation function:

$$\overline{\tau} = \arg\max_{\tau}\mathbb{E}\left\{u(t_k-\tau)y(t_k)\right\} \tag{40}$$

where $\mathbb{E}$ denotes mathematical expectation. For a causal system, the resulting $\overline{\tau}$ is normally larger than the true time delay, since it picks up not only the pure time delay, but also the system phase lag.

Algorithm 1:

Specify:

- $\overline{\tau}$, $\underline{\tau}$: upper and lower boundaries for τ;
- λ: breakpoint frequency of a state variable filter;
- $\{\tau_\ell = \ell h + \underline{\tau}\}_{\ell=0}^{L}$: time-delay grid, where L is a positive integer chosen such that $\tau_L \leqslant \overline{\tau}$.

Initialization:

1) Compute $\{U(\omega_k), Y(\omega_k)\}_{k=1}^{N}$ from the time-domain data using FFT.
2) Letting $F(i\omega_k) = 1/(i\omega_k+\lambda)^{n_a}$, compute $\tilde{Y}_F(\omega_k)$ in (26) and $\boldsymbol{\Phi}_F(\omega_k,\tau_0)$ in (27).
3) Compute an LS estimate of $\boldsymbol{\theta}$ as

$$\boldsymbol{\theta}(\tau_0) = \left(\sum_{k=1}^{N}\boldsymbol{\Phi}_F(\omega_k,\tau_0)\boldsymbol{\Phi}_F^\top(\omega_k,\tau_0)\right)^{-1}\times\sum_{k=1}^{N}\boldsymbol{\Phi}_F(\omega_k,\tau_0)\tilde{Y}_F(\omega_k).$$

Exhaustive search:

for $\ell = 1 : L$

1) Based on $\{\boldsymbol{\theta}(\tau_{\ell-1}),\tau_\ell\}$, update the filter $F(i\omega_k, \boldsymbol{\theta}(\tau_{\ell-1}))$ and the auxiliary model $G(i\omega_k,\boldsymbol{\theta}(\tau_{\ell-1}))$. Compute $\tilde{Y}_F(\omega_k)$ in (26), $\boldsymbol{\Phi}_F(\omega_k,\tau_\ell)$ in (27) and $\hat{\boldsymbol{\Phi}}_F(\omega_k)$ in (29).
2) Compute an IV estimate of $\boldsymbol{\theta}$ as

$$\boldsymbol{\theta}(\tau_\ell) = \left(\sum_{k=1}^{N}\hat{\boldsymbol{\Phi}}_F(\omega_k)\boldsymbol{\Phi}_F^\top(\omega_k,\tau_\ell)\right)^{-1}\sum_{k=1}^{N}\hat{\boldsymbol{\Phi}}_F(\omega_k)\tilde{Y}_F(\omega_k).$$

3) Compute $\breve{J}(\tau_\ell)$ in (32) by using $\boldsymbol{\theta}(\tau_\ell)$ and τ_ℓ.

end

Return the final estimates:

- The estimates to be returned are $\{\boldsymbol{\theta}(\tau_\Delta),\tau_\Delta\}$, where

$$\Delta = \arg\min_{\ell}\breve{J}(\tau_\ell).$$

2) *Choice of λ:* Low-pass filtering is an effective technique to smooth the loss function, and to help with global convergence, λ should be small, as suggested in [7]. Fortunately, since the time delay is searched on a grid in this paper, the choice of λ is not critical any more if the grid is sufficiently dense, so that global convergence can occur for a fairly wide range of values.
3) *Choice of h:* The loss function will have numerous local minima with respect to the time delay if aliasing occurs in the sampling process, each belonging to an interval of the sample time [6], [14]. In order to find out the global minimum effectively, it is better if the grid distance h is smaller than the sample time T, i.e., $h < T$.

D. Proposed Algorithm

The complete frequency-domain SRIVC method for transfer functions (TFFSRIVC) is summarized in Algorithm 2.

Algorithm 2: TFFSRIVC.

Specify:

- ς_{par}, ς_{fun}: tolerances of relative changes of τ and $\breve{J}(\tau)$;
- $\overline{\tau}$, $\underline{\tau}$: upper and lower boundaries for τ;
- λ: breakpoint frequency of a state variable filter;
- $\{\tau_\ell = \ell h + \underline{\tau}\}_{\ell=0}^{L}$: time-delay grid, where L is a positive integer chosen such that $\tau_L \leqslant \overline{\tau}$.

Initialization:

- Apply Algorithm 1 to generate initial values $\{\hat{\boldsymbol{\theta}}^0, \hat{\tau}^0\}$.

Iteration:

for $r = 0$: convergence

1) Based on $\{\hat{\boldsymbol{\theta}}^r, \hat{\tau}^r\}$, update the filter $F(i\omega_k, \hat{\boldsymbol{\theta}}^r)$ and the auxiliary model $G(i\omega_k, \hat{\boldsymbol{\theta}}^r)$. Compute $\tilde{Y}_F(\omega_k)$ in (26), $\boldsymbol{\Phi}_F(\omega_k, \hat{\tau}^r)$ in (27), $\hat{\boldsymbol{\Phi}}_F(\omega_k)$ in (29), $\hat{\Psi}(\omega_k)$ in (37) and $\Psi(\omega_k, \hat{\tau}^r)$ in (39). Compute the time-delay increment as
$$\Delta\hat{\tau}^r = \left(\nabla^2 \breve{J}(\hat{\tau}^r)\right)^{-1} \nabla \breve{J}(\hat{\tau}^r)$$
where $\nabla \breve{J}(\tau)$ and $\nabla^2 \breve{J}(\tau)$ are defined in (38).
2) Set $\mu^r = 1$ and perform the following:
   a) Let $\hat{\tau}^{r+1} = \hat{\tau}^r - \mu^r \Delta\hat{\tau}^r$. Do $\mu^r = \mu^r/2$ while $\hat{\tau}^{r+1} \notin [\underline{\tau}, \overline{\tau}]$. If $|\mu^r \Delta\hat{\tau}^r / \hat{\tau}^r| < \varsigma_{\text{par}}$, stop.
   b) Compute $\boldsymbol{\Phi}_F(\omega_k, \hat{\tau}^{r+1})$ and generate an estimate of $\boldsymbol{\theta}$
   $$\hat{\boldsymbol{\theta}}^{r+1} = \left(\sum_{k=1}^{N} \hat{\boldsymbol{\Phi}}_F(\omega_k) \boldsymbol{\Phi}_F^\top(\omega_k, \hat{\tau}^{r+1})\right)^{-1} \times \sum_{k=1}^{N} \hat{\boldsymbol{\Phi}}_F(\omega_k) \tilde{Y}_F(\omega_k).$$
   c) If $\breve{J}(\hat{\tau}^{r+1}) \geqslant \breve{J}(\hat{\tau}^r)$, let $\mu^r = \mu^r/2$ and go to Step 2.
3) If the following condition is satisfied, stop
$$\left|\breve{J}(\hat{\tau}^r) - \breve{J}(\hat{\tau}^{r+1})\right| / \breve{J}(\hat{\tau}^r) < \varsigma_{\text{fun}}.$$

end

E. Estimation Error Covariance Matrices

When the measurement noise is assumed to be white, once the parameter estimates converge, the estimation error covariance matrices of $\hat{\boldsymbol{\theta}}$ and $\hat{\tau}$ can be computed following from (31) and (38) as follows (see also [37]):

$$\boldsymbol{P}_{\hat{\boldsymbol{\theta}}} = \hat{\sigma}_E^2 \left(\sum_{k=1}^{N} \hat{\boldsymbol{\Phi}}_F(\omega_k) \hat{\boldsymbol{\Phi}}_F^\top(\omega_k)\right)^{-1} \tag{41a}$$

$$\boldsymbol{P}_{\hat{\tau}} = \hat{\sigma}_E^2 \left(\sum_{k=1}^{N} \hat{\Psi}(\omega_k)\, \hat{\Psi}^\top(\omega_k) - \sum_{k=1}^{N} \hat{\Psi}(\omega_k) \hat{\boldsymbol{\Phi}}_F^\top(\omega_k) \times \left(\sum_{k=1}^{N} \hat{\boldsymbol{\Phi}}_F(\omega_k) \hat{\boldsymbol{\Phi}}_F^\top(\omega_k)\right)^{-1} \sum_{k=1}^{N} \hat{\boldsymbol{\Phi}}_F(\omega_k)\, \hat{\Psi}^\top(\omega_k)\right)^{-1} \tag{41b}$$

where $\hat{\sigma}_E^2$ is the estimated variance of $E(\omega_k)$.

F. Extension for DT Model Estimation

The proposed TFFSRIVC can be slightly modified to estimate DT models with time delay. In this case, the input–output behavior of the system is characterized by a parameterized DT output-error model in the z transform operator

$$\begin{cases} x(t_k) = G(z, \boldsymbol{\eta}) u(t_k - \tau) = \dfrac{D(z, \boldsymbol{\eta})}{C(z, \boldsymbol{\eta})} u(t_k - \tau) \\ y(t_k) = x(t_k) + e(t_k) \end{cases} \tag{42}$$

where $\boldsymbol{\eta}$ is a vector of the rational model parameters

$$\boldsymbol{\eta} = [c_1, \ldots, c_{n_c}, d_1, \ldots, d_{n_d}]^\top \in \mathbb{R}^{n_c + n_d} \tag{43}$$

and polynomials $D(z, \boldsymbol{\eta})$ and $C(z, \boldsymbol{\eta})$ take the forms

$$D(z, \boldsymbol{\eta}) = d_1 z^{-1} + \cdots + d_{n_d} z^{-n_d} \tag{44a}$$

$$C(z, \boldsymbol{\eta}) = 1 + c_1 z^{-1} + \cdots + c_{n_c} z^{-n_c}, \quad n_c \geqslant n_d. \tag{44b}$$

Again, it is assumed that $C(z, \boldsymbol{\eta})$ and $D(z, \boldsymbol{\eta})$ are coprime, and that the roots of $D(z, \boldsymbol{\eta})$ are located within the unit cycle. Similar to (20), letting $z = \mathrm{e}^{i\omega_k T}$, (42) can have a frequency-domain formulation

$$Y(\omega_k) = G(\mathrm{e}^{i\omega_k T}, \boldsymbol{\eta}) \mathrm{e}^{-i\omega_k \tau} U(\omega_k) + E(\omega_k). \tag{45}$$

The unknown parameters $\boldsymbol{\eta}$ and τ in the above model can be estimated by using a procedure similar to the one presented in Sections III-A and III-B. However, the detailed derivation of a new algorithm is omitted, due to the length constraint of this paper. For clarity in the notation, the new method for estimating DT models with time delay is called frequency-domain simplified RIV method for transfer functions (TFFSRIV). A significant merit of TFFSRIV lies in that fractional time delays can be handled without any problem, since the shift operators have been replaced by the frequency variables. However, as some control design methodologies require the time delay to be an integer number of the sample time, to achieve this, it is suggested to perform a rounding operation only at the final iteration of the algorithm.

IV. Simulation Example

In this section, the analytical and data-driven modeling methods in Sections II and III are compared by means of numerical simulation in MATLAB (R2017b) on a 3.6-GHz quad-core desktop. The Simulink diagram used to generate data is shown in Fig. 4, with the main component parameters listed in Table I. In the acquisition of the output voltage, it is assumed that there is a 1-ms time delay when the measured output is transmitted from the sampler to the host computer via wireless communication. The dead band γ is set to zero.

Let $\alpha = \overline{\alpha} + \tilde{\alpha}$ and $V_o = \overline{V}_o + \tilde{v}_o$. For $\overline{\alpha} = 0.8\pi$ rad, the static output is $\overline{V}_o = 133.11$ V. To generate informative data for data-driven modeling, $\tilde{\alpha}$ is chosen as a cyclic pseudorandom binary sequence (PRBS) with amplitude switching between $\pm 0.02\pi$ rad. The shift register to generate the PRBS is of four stages and has a clock period of $100/f_s$, where f_s is

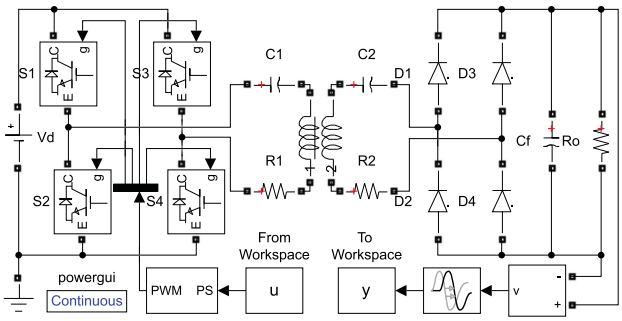

Fig. 4. Simulink diagram used for simulation study.

TABLE I
MAIN PARAMETERS OF THE SIMULINK DIAGRAM IN FIG. 4

Parameter	Explanation	Value
L_1	Inductance of the sending resonator	34 μH
L_2	Inductance of the receiving resonator	34 μH
M	Mutual inductance between L_1 and L_2	7.33 μH
C_1	Capacitance of the sending resonator	117 nF
C_2	Capacitance of the receiving resonator	117 nF
C_f	Capacitance of the output filter	300 μF
R_1	Equivalent resistance of the L_1, C_1 branch	0.039 Ω
R_2	Equivalent resistance of the L_2, C_2 branch	0.039 Ω
R_s	On-state resistance of the switches	0.001 Ω
R_o	Load resistance	5 Ω
V_r	Forward voltage of the diodes	0.8 V
V_d	Voltage of the DC source	400 V
f_s	Switching frequency of the inverter	80 kHz
τ	Communication delay	1 ms

the switching frequency of the inverter. The input to the system, $u(t_k) = \tilde{\alpha}(t_k)$, is sampled at $t_k = kT$, $k = 1, \ldots, 3200$, $T = 10/f_s$. In this setting, the duration of the experiment covers exactly 20 PRBS periods, as required by accurate frequency modeling (see Remark 4). Since noise is inevitable in the physical world, it is assumed that the measured output voltage is corrupted by white noise

$$y(t_k) = \tilde{v}_o(t_k) + e(t_k) \tag{46}$$

where the variance of $e(t_k)$ is suitably chosen such that the signal-to-noise ratio (SNR) is 15 dB. The SNR is defined as

$$\text{SNR} = 10 \log_{10}(P_{\tilde{v}}/P_e)\,\text{dB} \tag{47}$$

where $P_{\tilde{v}}$ and P_e are the power of $\tilde{v}_o(t_k)$ and $e(t_k)$, respectively. A portion of the input–output data is shown in Fig. 5.

The large-signal model of the system depicted in Fig. 4 can be established according to (10), whose output response can be simulated by using the method summarized in Algorithm 3. To obtain the small-signal model, the state vector of the large-signal model at the static operating point is required, which is, in fact, the steady-state response of the model to $\alpha = 0.8\pi$ rad when t_k tends to infinity, i.e., $\overline{\boldsymbol{X}} = \lim_{k\to\infty} \boldsymbol{X}(t_k)$. For the example considered in Fig. 4, we have

$$\overline{\boldsymbol{X}} = [46.91, 1.10, -3.90, 717.78, -0.23, 42.21, -797.58, -18.69, 134.41]^\top. \tag{48}$$

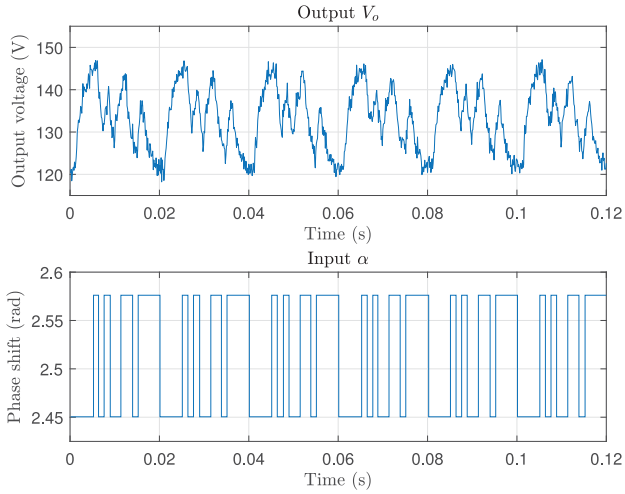

Fig. 5. Portion of sampled input–output data.

Algorithm 3:

for $k = 1 : N$

1 Construct $\{\boldsymbol{A}, \boldsymbol{B}, \boldsymbol{C}\}$ using the circuit component parameters according to (11). Then, compute the sampled data model matrices

$$\boldsymbol{A}_d = \mathrm{e}^{\boldsymbol{A}T}, \quad \boldsymbol{B}_d = \int_0^T \mathrm{e}^{\boldsymbol{A}t} dt\, \boldsymbol{B}$$

where T is the sample time. In the computation of $\boldsymbol{B}_d$, $\boldsymbol{B}$ is assumed to be zero-order hold.

2 Based on $\boldsymbol{x}(t_k)$, compute the output response at time instant t_{k+1} by

$$\begin{cases} \boldsymbol{x}(t_{k+1}) = \boldsymbol{A}_d \boldsymbol{x}(t_k) + \boldsymbol{B}_d \\ V_o(t_k) = \boldsymbol{C}\boldsymbol{x}(t_k). \end{cases}$$

Let $k = k + 1$ and go to step 1.

end

Based on the above $\overline{\boldsymbol{X}}$, a small-signal model can be derived according to (15). As discussed in Remark 3, the resulting small-signal model is of order nine and not suited to control design. Therefore, model reduction should be conducted to obtain a low-order model. Following from the idea of [12] and [41], a balanced realization of the small-signal model can be obtained using the MATLAB command

$$[\texttt{sysb}, \texttt{g}] = \texttt{balreal}(\texttt{sys});$$

For our example, the Gramian g is

$$\texttt{g} = [103.50, 13.83, 13.76, 0.08, 0.08, 0.06, 0.05, 0.04, 0.04]^\top \tag{49}$$

suggesting that a first-order model could give a satisfactory approximation of the original model. By using the MATLAB routine `modred`, the reduced first-order model in transfer function

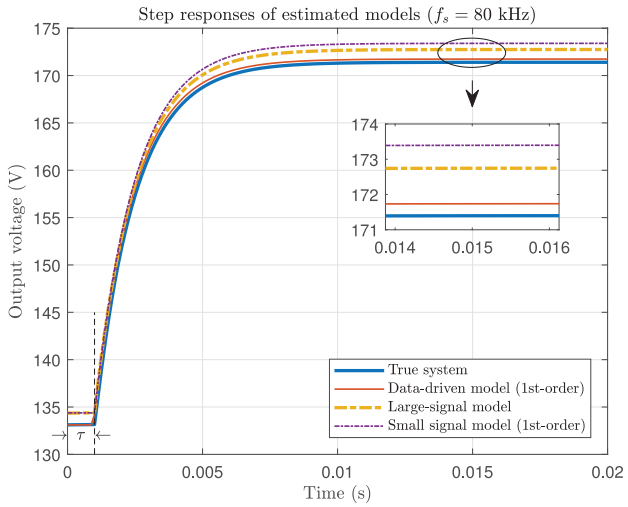

Fig. 6. Responses of the true system and estimated first-order models (50) and (51) to a step change of $\tilde{\alpha}$ from 0 to -0.06π rad around $\overline{\alpha} = 0.8\pi$ rad. The switching frequency is $f_s = 80$ kHz.

TABLE II
FIT RATIOS FOR THE ESTIMATED MODELS (50) AND (51)

Method	Model	fit
Analytical modeling	1st-order model (50)	80.29%
Data-driven modeling	1st-order model (51)	80.78%

form is presented as follows:

$$x(t) = \frac{-1.375 \times 10^5}{s + 664.3} u(t - 0.001). \tag{50}$$

Note that the analytical modeling method cannot estimate the time delay, and the true time delay $\tau = 0.001$ s is just used.

In what follows, TFFSRIVC is used to estimate the model parameters from the sampled data $\{y(t_k), u(t_k)\}_{k=1}^{3200}$, which is called by the statement

$$\begin{aligned} \texttt{model} = \texttt{tffsrivc}(\texttt{data}, n_a, n_b, \ldots \\ \texttt{'TdMax'}, \overline{\tau}, \texttt{'TdMin'}, \underline{\tau}, \ldots \\ \texttt{'Lambda'}, \lambda, \texttt{'TolPar'}, \varsigma_{\text{par}}, \ldots \\ \texttt{'TolFun'}, \varsigma_{\text{fun}}, \texttt{'NumTd'}, L) \end{aligned}$$

where `data` is an `iddata` object containing sampled input–output data. Using (40) to compute the upper time-delay boundary from sampled data yields $\overline{\tau} = 0.013$ s. Letting $\underline{\tau} = 0$ s, $\lambda = 10$ rad/s, $\varsigma_{\text{fun}} = \varsigma_{\text{par}} = 10^{-4}$, and generating 10 starting values for $\hat{\tau}^0$ uniformly distributed in the interval $[0, \overline{\tau}]$, the estimated first-order model based on a single run is

$$x(t) = \frac{-1.382 \times 10^5}{s + 674.4} u(t - 9.56 \times 10^{-4}). \tag{51}$$

To illustrate qualitatively the accuracy of the estimated models (50) and (51), their responses to a step change of $\tilde{\alpha}$ from 0 to -0.06π rad are computed around the operating point $\overline{\alpha} = 0.8\pi$ rad. The results are presented in Fig. 6, which shows that the step responses of the models generated by both the analytical and data-driven modeling methods are very close to the true system response, indicating that a first-order model is fairly enough to capture the basic behavior of the system. In addition, to quantify the explanatory ability of the estimated models (50) and (51), the fit ratio defined below is used as the performance index

$$\text{fit} = \left(1 - \frac{\|y(t_k) - y_s(t_k)\|_2}{\|y(t_k) - y_m(t_k)\|_2}\right) \times 100\% \tag{52}$$

where $y(t_k)$ and $y_s(t_k)$ stand for the sampled output and the simulated output by using the estimated model, respectively, and $y_m(t_k)$ is the mean of $y(t_k)$. It should be noted that, when SNR $= 15$ dB, the fit ratio has the following upper boundary:

$$\begin{aligned} \text{fit} &\leqslant \left(1 - \sqrt{P_e / (P_{\tilde{v}} + P_e)}\right) \times 100\% \\ &= \left(1 - 1/\sqrt{1 + 10^{-\text{SNR}/10}}\right) \times 100\% \\ &\approx 82.5\% \end{aligned} \tag{53}$$

where $P_{\tilde{v}}$ and P_e are defined in (47).

The fit ratios for the estimated models (50) and (51) are evaluated by the `compare` routine in MATLAB (see Table II). It is seen that analytical modeling yields 80.29%, while this value increases to 80.78% with data-driven modeling, showing an improvement of 0.49%, thanks to the data-driven mechanism that aims at minimizing the error between the measured and predicted outputs.

Next, let us consider the case when the operating frequency slightly deviates from the resonant frequency. The simulation settings remain the same as specified earlier in this section, except for the switching frequency, which is now changed to $f_s = 90$ kHz. In this case, the Gramian g is

$$\begin{aligned} \mathrm{g} = \big[&387.40, 293.15, 0.80, 0.64, 0.08, \\ &0.08, 0.06, 0.04, 0.04\big]^\top \end{aligned} \tag{54}$$

suggesting a second-order model for approximation. The result for the analytical modeling method is

$$x(t) = \frac{894.2s - 4.817 \times 10^9}{s^2 + 1414s + 2.556 \times 10^7} u(t - 0.001) \tag{55}$$

while the result for the data-driven modeling method is

$$x(t) = \frac{-6384s - 4.592 \times 10^9}{s^2 + 1647s + 2.486 \times 10^7} u(t - 0.001). \tag{56}$$

The responses of the above estimated models and the true system to a step change of $\tilde{\alpha}$ from 0 to -0.06π rad around $\overline{\alpha} = 0.8\pi$ rad are compared in Fig. 7. The corresponding fit ratios are listed in Table III.

It is interesting to observe from Fig. 7 that the step responses are oscillatory even though the switching frequency has been slightly increased. The reason can be explained as follows. When the resonant tank works at the resonant frequency, the coupling resonators can be seen as pure resistors. Then, the equivalent circuit has only one reactive component, i.e., C_f, and can thus be characterized by a first-order model. This is exactly the case of $f_s = 80$ kHz that has been previously considered. A first-order model has no oscillation component; therefore, the step response will monotonically increase or decrease, as shown in

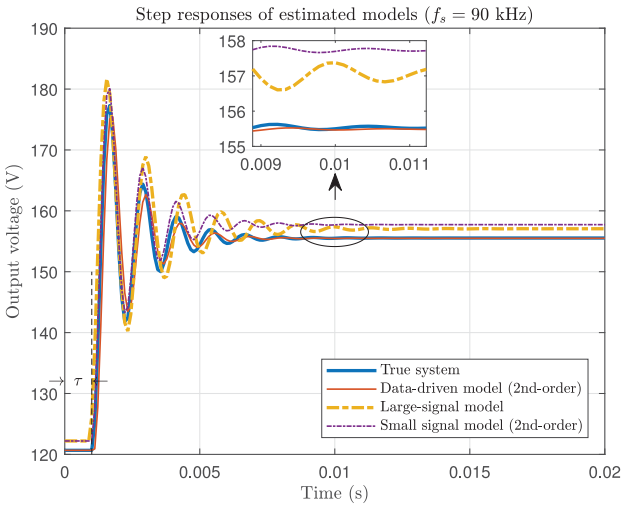

Fig. 7. Responses of the true system and estimated second-order models (55) and (56) to a step change of $\tilde{\alpha}$ from 0 to -0.06π rad around $\overline{\alpha} = 0.8\pi$ rad. The switching frequency is $f_s = 90$ kHz.

TABLE III
FIT RATIOS FOR THE ESTIMATED MODELS (55) AND (56)

Method	Model	fit
Analytical modeling	2nd-order model (55)	78.85%
Data-driven modeling	2nd-order model (56)	80.21%

Fig. 6. With this in mind, however, if the switching frequency is not equal to the resonant frequency, the resonant tank will be inductive if f_s is larger than the resonant frequency. In this regard, the whole circuit is equivalent to an LCR oscillator. This is the reason why (54) suggests a second-order model for approximation, and why oscillation is observed in Fig. 7.

In the presence of operating-resonant frequency mismatch, it is seen from Table III that the performance of the analytical modeling method declines, while the data-driven scheme remains still very good, giving rise to an improvement of 1.36% in the fit ratio compared to the analytical modeling method, which is better than the case of $f_s = 80$ kHz. These results confirm that the data-driven modeling method is able to provide accurate models even if the operating conditions have slightly drifted from the nominal ones.

V. EXPERIMENTAL VALIDATION

Let us now consider validation of the proposed data-driven modeling methods based on real data. The prototype of the WPT system used to generate experimental data is depicted in Fig. 8. Further details on the hardware configuration are given as follows.

1) *Controller:* To achieve improved reliability, the measurement and control are implemented on an NI CompartRIO system, which consists of a cRIO-9030 controller, an NI-9201 analog input module to sample the output voltage, and an NI-9401 high-speed digital input–output module to generate the control signals.
2) *Inverter:* The full-bridge inverter consists of four Infineon BSB056N10NN3 G MOSFETs and is powered by a 15-V dc voltage source. Each half-bridge leg is connected in parallel with a capacitor of 4.7 μF to suppress high-voltage spikes during MOSFET switchings. The timing sequence of MOSFET switchings are generated by the built-in field-programmable gate array of cRIO-9030.
3) *Resonant tank:* The two coupled coils, encapsulated in epoxy resin for waterproofing, have the same design parameters. Specifically, the number of turns is 19, the diameter is 40 cm, and the coil width is 7 cm. To alleviate the skin effect, the coils are made by Litz wire of 500 strands, each having a 0.1-mm diameter. The coils are axially aligned, with the gap distance being 60 cm. The equivalent resistances and the self- and mutual inductances of the coils are measured by an Agilent E4980A LCR meter at 300 kHz (see Table IV). Each coil is connected in series with a ceramic capacitor to compensate for the leakage inductance. Ideally, in order to have a resonant frequency of 300 kHz, the capacitors of the sending and receiving resonators should be 1.078 and 1.089 nF, respectively. However, due to the parasitic capacitances of the MOSFETs and rectifiers, experiments show that $C_1 = 1.00$ nF and $C_2 = 1.05$ nF are enough.
4) *Rectifier bridge:* The rectifier bridge consists of four SS34 Schottky barrier rectifiers. In order to attenuate various types of ripples in the output voltage, three types of capacitors, namely, an electrolytic capacitor of 470 μF, a polypropylene capacitor of 1 μF, and two ceramic capacitors of 100 nF, are connected in parallel with the rectifier bridge.

TABLE IV
MAIN PARAMETERS OF THE EXPERIMENTAL APPARATUS

Parameter	Explanation	Value
L_1	Inductance of the sending resonator	261.2 μH
L_2	Inductance of the receiving resonator	258.4 μH
M	Mutual inductance between L_1 and L_2	3.242 μH
C_1	Capacitance of the sending resonator	1.000 nF
C_2	Capacitance of the receiving resonator	1.050 nF
C_f	Capacitance of the output filter	471.2 μF
R_1	Equivalent resistance of the L_1, C_1 branch	0.941 Ω
R_2	Equivalent resistance of the L_2, C_2 branch	0.959 Ω
R_s	On-state resistance of the switches	0.005 Ω
R_o	Load resistance	10 Ω
V_r	Forward voltage of the diodes	0.5 V
V_d	Voltage of the DC source	15 V
f_s	Switching frequency of the inverter	300 kHz
γ	Dead band	75 ns

The experimental apparatus is a computer-controlled system, whose input, i.e., the phase shift of the inverter α, is specified by the experimenter and thus is *a priori* known. In this framework, the only signal that needs to be sampled through analog-to-digital conversion is the output voltage V_o. For simplicity of experiment design, sampling of the output voltage is done on the host computer side, rather than a remote device with data transferred to the host computer via wireless communication. As a result, the time delay will be relatively small due to the absence of communication delays.

The experimental data for data-driven modeling are collected along with a procedure similar to that in Section IV. Letting $\overline{\alpha} = 0.7879\pi$ rad, the steady-state output voltage is obtained as $\overline{V}_o = 2.5453$ V. The small signal $\tilde{\alpha}$ is chosen as a PRBS of

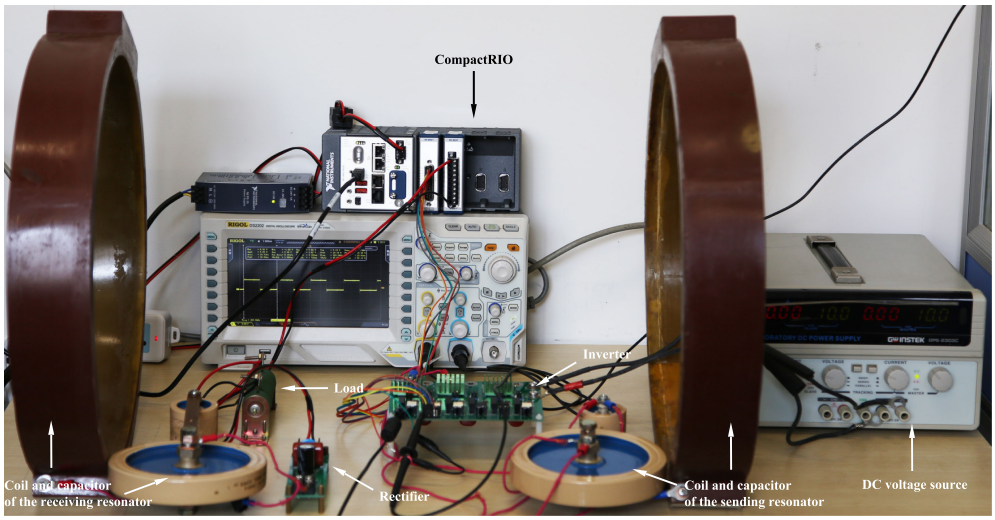

Fig. 8. Prototype of the WPT system.

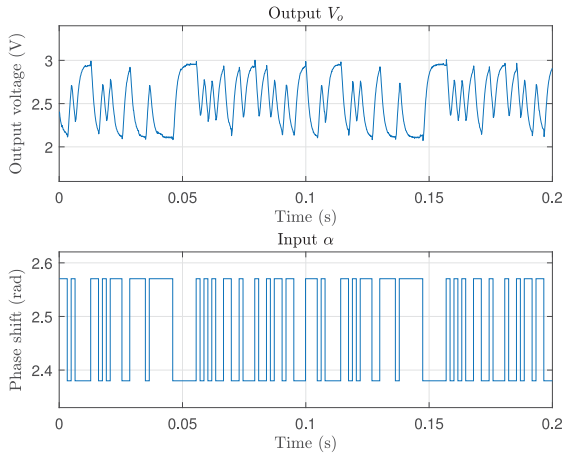

Fig. 9. Portion of input–output data obtained from NI CompactRIO.

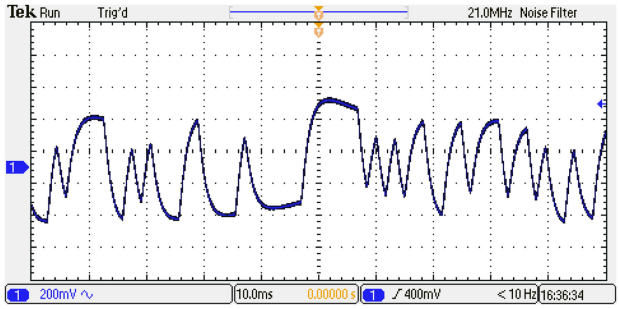

Fig. 10. Snapshot of the output voltage V_o captured by an oscilloscope.

amplitude switching between $\pm 0.0303\pi$ rad, which is generated from a six-stage shift register of clock period 1.584×10^{-3} s. The output voltage is sampled at time instant $t_k = kT$, where $k = 1, \ldots, 10240$ and $T = 9.9 \times 10^{-5}$ s. The data can be accessed via LabVIEW (version 2018) on the host computer; see Fig. 9 for a portion of the sampled input–output data. The signals in the circuit are also observed by a Tektronix DPO2004B oscilloscope; see Fig. 10 for a snapshot of the output voltage V_o, which corresponds to the one in the top panel of Fig. 9 up to

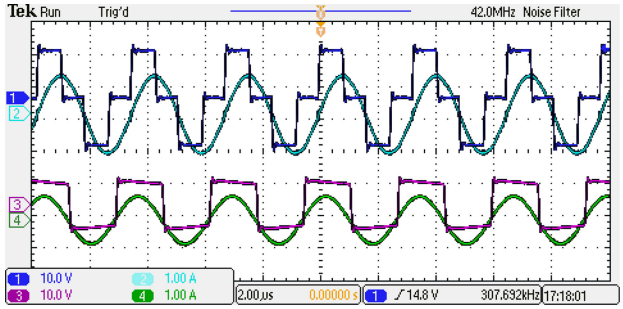

Fig. 11. Snapshot of the signals in the resonant tank for $\alpha \approx 0.5\pi$ rad. Curves 1–4 denote, respectively, the input voltage v_1, the input current i_1, the output voltage v_2, and the output current i_2 of the resonant tank.

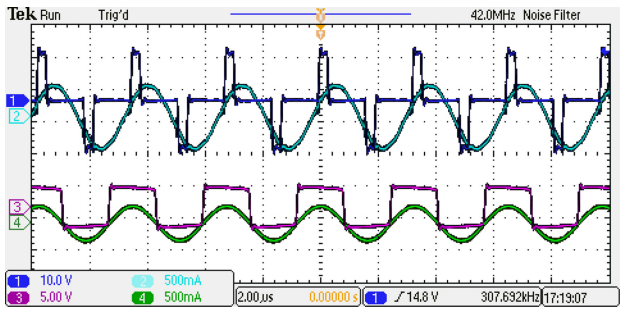

Fig. 12. Snapshot of the signals in the resonant tank for $\alpha \approx 0.8\pi$ rad. Curves 1–4 denote, respectively, the input voltage v_1, the input current i_1, the output voltage v_2, and the output current i_2 of the resonant tank.

$t = 0.1$ s, and Figs. 11 and 12 for a snapshot of the signals in the resonant tank: the input voltage v_1 and current i_1, and the output voltage v_2 and current i_2.

To show the statistical properties of the parameter estimates, a Monte–Carlo (MC) experiment of 30 runs is conducted, which gives rise to 30 different datasets. For the TFFSRIVC and TFFSRIV methods, the hyperparameters are chosen as: $\underline{\tau} = 0$ s, $\overline{\tau} = 0.001$ s, $\lambda = 10$ rad/s, and $\varsigma_{\text{fun}} = \varsigma_{\text{par}} = 10^{-4}$. To reliably initialize the time delay, a set of 40 initial values uniformly distributed in the interval $[0, \overline{\tau}]$ is used. The transfer function estimation (TFEST) routine from the MATLAB system

TABLE V
ESTIMATED CT MODEL PARAMETERS

Method	(n_a, n_b)	Estimated CT model parameters (mean ($\pm$std))					$\overline{\text{fit}}$	$\overline{N}_{\text{iter}}$	$\overline{T}_{\text{c}}$
		$\hat{a}_1$	$\hat{a}_2$	$\hat{b}_0$	$\hat{b}_1$	$\hat{\tau}$			
TFEST	(1, 0)	756.18 ($\pm$0.87)	— —	-3478.7 ($\pm$6.1)	— —	0.000297 ($\pm$0)	92.55%	10.0	1.33 s
	(2, 0)	2761.0 ($\pm$7.2)	1.9142×10^6 ($\pm 4.6 \times 10^3$)	-8.5050×10^6 ($\pm 2.55 \times 10^4$)	— —	0 ($\pm$0)	94.08%	9.3	1.27 s
	(2, 1)	4248.1 ($\pm$30.3)	3.0730×10^6 ($\pm 2.27 \times 10^4$)	1977.3 ($\pm$30.7)	-1.3605×10^7 ($\pm 8.9 \times 10^4$)	0 ($\pm$0)	96.45%	7.1	1.14 s
TFFSRIVC	(1, 0)	816.08 ($\pm$0.94)	— —	-3672.8 ($\pm$6.4)	— —	0.00036216 ($\pm 1 \times 10^{-8}$)	94.38%	1.0	0.10 s
	(2, 0)	4291.5 ($\pm$13.8)	3.1361×10^6 ($\pm 1.06 \times 10^4$)	-1.3949×10^7 ($\pm 5.8 \times 10^4$)	— —	0.00014504 ($\pm 5.5 \times 10^{-7}$)	96.00%	1.1	0.12 s
	(2, 1)	4380.6 ($\pm$49.1)	3.1891×10^6 ($\pm 4.22 \times 10^4$)	1503.9 ($\pm$141.9)	-1.4161×10^7 ($\pm 1.73 \times 10^5$)	4.4110×10^{-5} ($\pm 1.2811 \times 10^{-5}$)	96.29%	1.7	0.16 s

$\overline{\text{fit}}$—Mean fit value. $\overline{N}_{\text{iter}}$—Mean iteration number. $\overline{T}_c$—Mean computing time for a single run.

TABLE VI
ESTIMATED DT MODEL PARAMETERS

Method	(n_c, n_d)	Estimated DT model parameters (mean ($\pm$std))					$\overline{\text{fit}}$	$\overline{N}_{\text{iter}}$	$\overline{T}_{\text{c}}$
		$\hat{c}_1$	$\hat{c}_2$	$\hat{d}_1$	$\hat{d}_2$	$\hat{\tau}$			
TFEST	(1, 1)	-0.92815 ($\pm 8 \times 10^{-5}$)	— —	-0.33085 ($\pm$0.00057)	— —	0.000297 ($\pm$0)	92.54%	3.0	0.29 s
	(2, 1)	-1.7675 ($\pm$0.0005)	0.78221 ($\pm$0.00048)	-0.065285 ($\pm$0.000169)	— —	0 ($\pm$0)	92.99%	5.8	0.22 s
	(2, 2)	-1.6348 ($\pm$0.0021)	0.65917 ($\pm$0.00197)	0.095901 ($\pm$0.001938)	-0.20377 ($\pm$0.00245)	0 ($\pm$0)	96.46%	4.0	0.24 s
TFFSRIV	(1, 1)	-0.91935 ($\pm 9 \times 10^{-5}$)	— —	-0.35802 ($\pm$0.00062)	— —	0.000396 ($\pm$0)	93.92%	2.0	0.13 s
	(2, 1)	-1.6206 ($\pm$0.0011)	0.64618 ($\pm$0.00100)	-0.11369 ($\pm$0.00037)	— —	0.000198 ($\pm$0)	96.02%	3.8	0.16 s
	(2, 2)	-1.6346 ($\pm$0.0021)	0.65897 ($\pm$0.00197)	0.096128 ($\pm$0.001938)	-0.20405 ($\pm$0.00245)	0 ($\pm$0)	96.46%	4.6	0.17 s

$\overline{\text{fit}}$—Mean fit value. $\overline{N}_{\text{iter}}$—Mean iteration number. $\overline{T}_c$—Mean computing time for a single run.

identification toolbox is also tested to provide a comparison study. TFEST can be configured to estimate either CT or DT models with time delay. To enable the CT model estimation function, the following commands are used:

$$\begin{aligned}
\texttt{opt} &= \texttt{tfestOptions};\\
\texttt{num} &= \texttt{ones}(1, \texttt{nb}) \star \texttt{NaN};\\
\texttt{den} &= [1, \texttt{ones}(1, \texttt{na}) \star \texttt{NaN}];\\
\texttt{sys0} &= \texttt{idtf}(\texttt{num}, \texttt{den}, '\texttt{IODelay}', \texttt{NaN});\\
\texttt{sys} &= \texttt{tfest}(\texttt{data}, \texttt{sys0}, \texttt{opt});
\end{aligned}$$

To enable the DT model estimation function, the commands are the same except for `sys0`, which should be generated as

$$\texttt{sys0} = \texttt{idtf}(\texttt{num}, \texttt{den}, \texttt{T}, '\texttt{IODelay}', \texttt{NaN});$$

where `T` is the sample time.

Based on the circuit component parameters available from the manufacturer's data sheets (see Table IV), the Gramian of the small-signal model is obtained as

$$\begin{aligned}
\texttt{g} = \big[&0.24, 0.01, 0.01, 0.00, 0.00,\\
&0.00, 0.00, 0.00, 0.00\big]^\top
\end{aligned} \tag{57}$$

indicating a first-order model for approximation. However, to show how accurate the first-order model can be, several pairs of degree values for (n_a, n_b) and (n_c, n_d) are compared.

The mean values and standard deviations of the parameter estimates, computed from the 30 MC realizations, are listed in Tables V and VI, showing that all the estimated models are very accurate (fit $> 92\%$). As the output voltage is sampled by cRIO-9030 directly, there is no communication delay, and thus, the estimated time delays are relatively small. For example, in the first-order CT model generated by TFFSRIVC, we have $\hat{\tau} = 3.622 \times 10^{-4}$ s, which is only 3.658 times of the sample time $T = 9.9 \times 10^{-5}$ s. More remarks regarding these experimental results are presented in the following.

1) When the number of model parameters increases, the fit ratio becomes higher (from 94.38% to 96.29% in the TFFSRIVC case), and the estimated time delay becomes smaller (from 3.6×10^{-4} to 4.4×10^{-5} s in the TFFSRIVC case). The first phenomenon is quite reasonable since a model of more parameters provides more freedom to fit the data. For the latter, it should be noted that a small time delay can be approximated by a rational transfer function [18], and in view of this, the required amount of pure time delay can be reduced if the model order becomes higher.

2) TFEST yields a time delay that is an integer number of the sample time. From the MATLAB help document, we should be aware of the rationale behind TFEST to estimate the time delay—it first compares an autoregressive exogenous model with different integer time delays and then picks the best as the final time delay estimate. Subsequently, a nonlinear LS method is adopted to iteratively update the linear model parameters by setting the time delay to the previous estimate. In addition, since the time delay is fixed and known in estimating the rational model parameters, the associated parameter estimation error covariances can be reduced. This explains why the standard deviations of TFEST are smaller than that of TFFSRIVC.
3) The proposed frequency-domain algorithms converge very fast, typically within 0.17 s and five iterations. This reason can be explained as follows: as the sampled data have a low noise level, evidenced from Fig. 9, the initial model obtained by the LS estimator in the initialization step of Algorithm 2 can be accurate if the time-delay grid is sufficiently dense (the example considered falls into this situation). Starting from such an accurate initial model, the rate of convergence can be accelerated.

VI. Conclusion

Inferring mathematical models for WPT systems has been investigated in this paper. Two methods to handle this problem have been considered. One is the analytical modeling method, which has been well known in the field of power electronics. It has been shown that the resulting small-signal model can provide good insights into the system behavior at a steady-state point, if the true circuit parameters are exactly known. Otherwise, the model accuracy may decline. To relax the dependence on the knowledge of the true circuit parameters, a data-driven modeling method has been proposed, with the main idea being to estimate model parameters by minimizing the mean-squared error between the sampled output and the model output. This method is based on sampled input–output data, which are easy to obtain and, therefore, is more suitable for dynamic model tracking. However, in the application of this data-driven approach, one needs to specify the model order. As the circuit topology and nominal component parameters are normally *a priori* known, a new procedure has been proposed that is a combination of the analytical and data-driven modeling methods, i.e., using the former to determine the model structure while using the latter to estimate the model parameters. Numerical simulation has shown that the proposed method is very accurate: for the considered simulation example, it achieves an 80.78% fit ratio for a 15-dB SNR, which is very close to the upper performance bound 82.5%. Experimental results have shown its fast convergence rate: for a dataset of 10 240 samples with a 1.0138 s duration, the algorithm converges within 0.17 s in second-order modeling, yielding a fit ratio up to 96.46%.

References

[1] S. Ahmed, B. Huang, and S. L. Shah, "Parameter and delay estimation of continuous-time models using a linear filter," *J. Process Control*, vol. 16, no. 4, pp. 323–331, 2006.

[2] B. L. Cannon, J. F. Hoburg, D. D. Stancil, and S. C. Goldstein, "Magnetic resonant coupling as a potential means for wireless power transfer to multiple small receivers," *IEEE Trans. Power Electron.*, vol. 24, no. 7, pp. 1819–1825, Jul. 2009.

[3] F. Chen, H. Garnier, and M. Gilson, "Robust identification of continuous-time models with arbitrary time-delay from irregularly sampled data," *J. Process Control*, vol. 25, pp. 19–27, 2015.

[4] F. Chen, H. Garnier, M. Gilson, and X. Zhuan, "Frequency domain identification of continuous-time output-error models with time-delay from relay feedback tests," *Automatica*, vol. 98, pp. 180–189, 2018.

[5] F. Chen, H. Garnier, A. Padilla, and M. Gilson, "Recursive IV identification of continuous-time models with time delay from sampled data," *IEEE Trans. Control Syst. Technol.*, to be published.

[6] F. Chen, M. Gilson, H. Garnier, and T. Liu, "Robust time-domain output error method for identifying continuous-time systems with time delay," *Syst. Control Lett.*, vol. 102, pp. 81–92, 2017.

[7] F. Chen, X. Zhuan, H. Garnier, and M. Gilson, "Issues in separable identification of continuous-time models with time-delay," *Automatica*, vol. 94, pp. 258–273, 2018.

[8] D. Czarkowski and M. K. Kazimierczuk, "Phase-controlled series-parallel resonant converter," *IEEE Trans. Power Electron.*, vol. 8, no. 3, pp. 309–319, Jul. 1993.

[9] D. Czarkowski and M. K. Kazimierczuk, "Single-capacitor phase-controlled series resonant converter," *IEEE Trans. Circuits Syst.*, vol. 40, no. 6, pp. 383–391, Jun. 1993.

[10] Q. Deng *et al.*, "Edge position detection of on-line charged vehicles with segmental wireless power supply," *IEEE Trans. Veh. Technol.*, vol. 66, no. 5, pp. 3610–3621, May 2017.

[11] Q. Deng *et al.*, "Frequency-dependent resistance of Litz-wire square solenoid coils and quality factor optimization for wireless power transfer," *IEEE Trans. Ind. Electron.*, vol. 63, no. 5, pp. 2825–2837, May 2016.

[12] Q. Deng *et al.*, "Modeling and control of inductive power transfer system supplied by multiphase phase-controlled inverter," *IEEE Trans. Power Electron.*, to be published.

[13] Z. Fang, J. Wang, S. Duan, K. Liu, and T. Cai, "Control of an LLC resonant converter using load feedback linearization," *IEEE Trans. Power Electron.*, vol. 33, no. 1, pp. 887–898, Jan. 2018.

[14] G. Ferretti, C. Maffezzoni, and R. Scattolini, "On the identifiability of the time delay with least-squares methods," *Automatica*, vol. 32, no. 3, pp. 449–453, 1996.

[15] H. Garnier, "Direct continuous-time approaches to system identification. Overview and benefits for practical applications," *Eur. J. Control*, vol. 24, pp. 50–62, 2015.

[16] H. Garnier and L. Wang, Eds., *Identification of Continuous-Time Models From Sampled Data*. London, U.K.: Springer-Verlag, 2008.

[17] H. Garnier and P. C. Young, "The advantages of directly identifying continuous-time transfer function models in practical applications," *Int. J. Control*, vol. 87, no. 7, pp. 1319–1338, 2014.

[18] P. J. Gawthrop and M. T. Nihtilä, "Identification of time-delays using a polynomial identification method," *Syst. Control Lett.*, vol. 5, no. 4, pp. 267–271, 1985.

[19] M. Gilson, J. S. Welsh, and H. Garnier, "A frequency localizing basis function-based IV method for wideband system identification," *IEEE Trans. Control Syst. Technol.*, vol. 26, no. 1, pp. 329–335, Jan. 2018.

[20] S. Y. R. Hui, W. Zhong, and C. K. Lee, "A critical review of recent progress in mid-range wireless power transfer," *IEEE Trans. Power Electron.*, vol. 29, no. 9, pp. 4500–4511, Sep. 2014.

[21] M. K. Kazimierczuk, D. Czarkowski, and N. Thirunarayan, "A new phase-controlled parallel resonant converter," *IEEE Trans. Power Electron.*, vol. 40, no. 6, pp. 542–552, Dec. 1993.

[22] A. Kurs, A. Karalis, R. Moffatt, J. D. Joannopoulos, P. Fisher, and M. Soljačić, "Wireless power transfer via strongly coupled magnetic resonances," *Science*, vol. 317, no. 83, pp. 83–86, 2007.

[23] H. Li, K. Wang, L. Huang, W. Chen, and X. Yang, "Dynamic modeling based on coupled modes for wireless power transfer systems," *IEEE Trans. Power Electron.*, vol. 30, no. 11, pp. 6245–6253, Nov. 2015.

[24] L. Ljung, *System Identification—Theory for the User*. Upper Saddle River, NJ, USA: Prentice-Hall, 1999.

[25] L. Ljung, "Identification for control: Simple process models," in *Proc. 41st IEEE Conf. Decis. Control*, Las Vegas, NV, USA, Dec. 2002, pp. 4652–4657.

[26] F. Musavi and W. Eberle, "Overview of wireless power transfer technologies for electric vehicle battery charging," *IET Power Electron.*, vol. 7, no. 1, pp. 60–66, 2014.

[27] R. Pintelon and J. Schoukens, *System Identification: A Frequency Domain Approach*. Hoboken, NJ, USA: Wiley–IEEE Press, 2012.

[28] A. P. Sample, D. A. Meyer, and J. R. Smith, "Analysis, experimental results, and range adaptation of magnetically coupled resonators for wireless power transfer," *IEEE Trans. Ind. Electron.*, vol. 58, no. 2, pp. 544–554, Feb. 2011.
[29] J. Schoukens, Y. Rolain, and R. Pintelon, "Analysis of windowing/leakage effects in frequency response function measurements," *Automatica*, vol. 42, pp. 27–38, 2006.
[30] T. Söderström and P. Stoica, *Instrumental Variable Methods for System Identification*. New York, NY, USA: Springer-Verlag, 1983.
[31] T. Söderström and P. Stoica, *System Identification* (Series in Systems and Control Engineering). Englewood Cliffs, NJ, USA: Prentice-Hall, 1989.
[32] C. Song *et al.*, "EMI reduction methods in wireless power transfer system for drone electrical charger using tightly coupled three-phase resonant magnetic field," *IEEE Trans. Ind. Electron.*, vol. 65, no. 9, pp. 6839–6849, Sep. 2018.
[33] A. K. Swain, M. J. Neath, U. K. Madawala, and D. J. Thrimawithana, "A dynamic multivariable state-space model for bidirectional inductive power transfer systems," *IEEE Trans. Power Electron.*, vol. 27, no. 11, pp. 4772–4780, Nov. 2012.
[34] V. Valdivia, A. Barrado, A. Lázaro, P. Zumel, C. Raga, and C. Fernández, "Simple modeling and identification procedures for 'black-box' behavioral modeling of power converters based on transient response analysis," *IEEE Trans. Power Electron.*, vol. 24, no. 12, pp. 2776–2790, Dec. 2009.
[35] Z. Yang, H. Iemura, S. Kanae, and K. Wada, "Identification of continuous-time systems with multiple unknown time delays by global nonlinear least-squares and instrumental variable methods," *Automatica*, vol. 43, no. 7, pp. 1257–1264, 2007.
[36] P. C. Young, *Recursive Estimation and Time-series Analysis: An Introduction for the Student and Practitioner*. Berlin, Germany: Springer-Verlag, 2011.
[37] P. C. Young, "Refined instrumental variable estimation: Maximum likelihood optimization of a unified Box–Jenkins model," *Automatica*, vol. 51, no. 1, pp. 35–46, 2015.
[38] P. C. Young and A. Jakeman, "Refined instrumental variable methods of recursive time-series analysis: Part I, single input, single output systems," *Int. J. Control*, vol. 29, no. 1, pp. 1–30, 1979.
[39] Z. U. Zahid *et al.*, "Modeling and control of series–series compensated inductive power transfer system," *IEEE J. Emerg. Sel. Topics Power Electron.*, vol. 3, no. 1, pp. 111–123, Mar. 2015.
[40] K. Zhang, Z. Shan, and J. Jatskevich, "Large- and small-signal average-value modeling of dual-active-bridge DC-DC converter considering power losses," *IEEE Trans. Power Electron.*, vol. 32, no. 3, pp. 1964–1974, Mar. 2017.
[41] S. Zheng and D. Czarkowski, "Modeling and digital control of a phase-controlled series-parallel resonant converter," *IEEE Trans. Ind. Electron.*, vol. 54, no. 2, pp. 707–715, Apr. 2007.

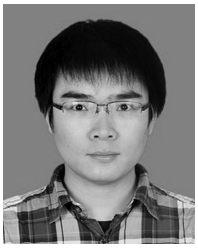

Fengwei Chen was born in Chongqing, China. He received the B.Eng. and M.Eng. degrees from Wuhan University, Wuhan, China, in 2009 and 2011, respectively, and the Ph.D. degree from the Université de Lorraine, Nancy, France, in 2014.

He was a Lecturer with the Dalian University of Technology, Dalian, China, till 2016. He is currently a Postdoctoral Researcher with Wuhan University. His research interests include system identification, parameter estimation, and wireless power transfer.

Hugues Garnier has been a Professor of Control Theory and Applications with the University of Lorraine, Nancy, France, since 2003. He was a Visiting Researcher with the University of Newcastle, Australia, in 2002–2003 and with the University of California, San Diego, CA, USA, in 2012–2013. Since 2000, he has been very active in promoting direct continuous-time model-based approaches to system identification. He was the Editor of two books and was the Guest Editor for three special issues of international journals. He is also behind CONTSID, a noncommercial MATLAB toolbox for continuous-time system identification. His main research interests include system identification. His current applications include problems such as data-based modeling for battery management systems, satellite attitude control, or large flexible space structure control.

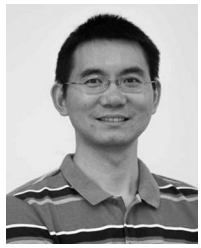

Qijun Deng received the B.S. and M.Sc. degrees in mechanical engineering in 1999 and 2002, respectively, and the Ph.D. degree in computer application technology in 2005, all from Wuhan University, Wuhan, China.

In June 2005, he joined the Department of Automation (which is now merged into the School of Electrical Engineering and Automation), Wuhan University, where he is currently a Professor. From 2013 to 2014, he was a Visiting Scholar with the New York University Tandon School of Engineering. His research interests include wireless power transfer, distribution automation, and electrical power informatics.

Marian K. Kazimierczuk (M'91–SM'91–F'04) received the M.S., Ph.D., and D.Sci. degrees in electronics engineering from the Department of Electronics, Warsaw University of Technology, Warsaw, Poland, in 1971, 1978, and 1984, respectively.

From 1972 to 1978, he was a Teaching and Research Assistant with the Department of Electronics, Institute of Radio Electronics, Warsaw University of Technology, where he was an Assistant Professor from 1978 to 1984. In 1984, he was a Project Engineer with Design Automation Inc., Lexington, MA, USA. In 1984/1985, he was a Visiting Professor with the Department of Electrical and Computer Engineering, Virginia Polytechnic Institute and State University, Blacksburg, VA, USA. Since 1985, he has been with the Department of Electrical Engineering, Wright State University, Dayton, OH, USA, where he is currently a University Distinguished Professor. He is the author/co-author of 210 peer-reviewed journal papers and 260 conference papers and holds eight patents. He is also the author/co-author of seven books entitled *Electronic Devices: A Design Approach* (Englewood Cliffs, NJ, USA: Prentice-Hall/Pearson, 2004), *Laboratory Manual for Electronic Devices: A Design Approach* (Englewood Cliffs, NJ, USA: Prentice-Hall/Pearson, 2004), *Resonant Power Converters* (2nd ed. Hoboken, NJ, USA: Wiley, 2011), *Pulse-Width Modulated DC-DC Power Converters* (2nd ed. Hoboken, NJ, USA: Wiley, 2016), *Laboratory Manual for Pulse-Width Modulated DC-DC Power Converters* (Hoboken, NJ, USA: Wiley, 2016), *High-Frequency Magnetic Components* (2nd ed. Hoboken, NJ, USA: Wiley, 2014), and *RF Power Amplifiers* (2nd ed. Hoboken, NJ, USA: Wiley, 2015). His research interests include high-frequency high-efficiency switching-mode tuned power amplifiers, resonant and pulsewidth modulated dc–dc power converters, dc–ac inverters, high-frequency soft-switching rectifiers, electronic ballasts, modeling and control of converters, new converter topologies, gate drivers, high-frequency magnetics, wireless power transfer, renewable energy sources, power factor correction, and wide-bandgap power semiconductor devices.

Dr. Kazimierczuk has served as an Associate Editor for the IEEE TRANSACTIONS ON CIRCUITS AND SYSTEMS and the *Journal of Circuits, Systems, and Computers*, and serves as an Associate Editor for the IEEE TRANSACTIONS ON INDUSTRIAL ELECTRONICS, the *International Journal of Circuits Theory and Applications*, and *IET Circuits, Devices, and Systems*. He was the recipient of the Best Paper Award from *IET Power Electronics* in 2012. He has received Presidential Research, Teaching, and Service Awards as well as the Trustee's Award from Wright State University.

Xiangtao Zhuan received the B.Eng. degree from the Wuhan University of Hydraulic and Electrical Engineering, Wuhan, China, in 1999, the master's degree from Wuhan University, Wuhan, in 2002, and the Ph.D. degree from the University of Pretoria, Pretoria, South Africa, in 2007.

He is currently a Professor with Wuhan University, where he is the Vice-Dean of the School of Electrical Engineering and Automation. His research interests include modeling and optimal control involving in power systems, heavy-haul trains, and industrial processes.